BALM: Watching the Formation of Tethered Bilayer Lipid Membranes with Submicron Lateral Resolution

J. Bompard, O. Maniti, R. Aboukhachfe, D. Ausserre, A. Girard-Egrot

BALM: Watching the Formation of Tethered Bilayer Lipid Membranes with submicron lateral resolution

J. BOMPARD[1], O. MANITI[1], R. ABOUKHACHFE[2], D. AUSSERRE[3]*, A. GIRARD-EGROT[1]*
Affiliations:
[1] Univ Lyon, Université Claude Bernard Lyon 1, CNRS, Institut de Chimie et Biochimie Moléculaires et Supramoléculaires, ICBMS, UMR 5246, GEMBAS Team, Lederer building, 1 rue Victor Grignard, F-69622 Villeurbanne , France
[2] Lebanese university, Faculty of technology, Hisbe Street, Saida, Lebanon
[3] Institut Molecules & Matériaux du Mans, IMMM CNRS UMR 6283, Le Mans Université, Avenue Olivier Messiaen, 72085 Le Mans.

*: Co-corresponding authors agnes.girard-egrot@univ-lyon1.fr and Dominique.Ausserre@univ-lemans.fr

RUNNING TITLE

BALM for live characterization of tBLM
Key words: Biomimetic membranes, Peptide Tethered Bilayers, BALM, SPR, membrane formation.

ABSTRACT

Tethered Bilayer Lipid Membranes (tBLMs) are artificial membranes largely used for the *in-situ* study of biological membranes and membrane-associated proteins. Up to now, the formation of these membranes was essentially monitored by surface averaging techniques like SPR and QCM-D which cannot provide both local and real-time information in a single approach. Here, we report an original application of Backside Absorbing Layer Microscopy (BALM), a novel white-light wide-field optical microscopy, to study tBLMs. Thanks to the combination of sensitivity and resolution, BALM not only allowed the real-time quantitative monitoring of the tBLM formation, but it also enabled the high-resolution visualization of the local fluxes and matter exchanges taking place at each step of the process. Quantitative BALM measurements of the final layer thickness, reproduced in parallel with SPR, were consistent with the achievement of a continuous lipid bilayer. This finding was confirmed with BALM imaging, which additionally revealed the heterogeneity of the bilayer during its formation. While established real-time techniques, like SPR or QCM-D, view the surface as homogeneous, BALM showed the presence of surface patterns appearing in the first step of the tBLM formation process and governing every thereafter matter adsorption and desorption. Finally, matter fluxes persisting even after rinsing at the end of the tBLM formation demonstrated the lasting presence of dispersed vesicular pockets with laterally-fluctuating positions over the final single and continuous lipid bilayer. These new mechanistic insights on the tBLM formation process demonstrate the great potential of BALM in the study of complex biological systems.

INTRODUCTION

As the interphase between the cell and its environment, biological membranes not only serve as physical boundaries, but they also host a plethora of membrane proteins. These proteins assume many cell functions such as cell-to-cell communication, nutrient import, or signal transduction and, as such, they are the target of more than 60% of medicinal drugs.[1–3] Investigating membranes and membrane proteins is therefore of critical importance. However, due to the complexity of the cell, *in situ* investigation of biological membranes remains a great challenge. Biomimetic membrane platforms in which a synthetic membrane is supported by a solid surface are hence used either for membrane property measurements or the *in vitro* reconstitution and study of membrane proteins. Various biomimetic membranes have been developed, such as solid-supported membranes [4,5], polymer-cushioned membranes [6–8], hybrid lipid bilayers [9–11], suspended lipid bilayers [12–14], and tethered bilayer lipid membranes or tBLMs.[15–23]

tBLMs are a natural progression from the planar supported lipid bilayers (SLBs). As first reported by McConnell *et al.* [5], SLBs are classically obtained by spreading small unilamellar vesicles on hydrophilic solid supports [24–27], which results in a lipid bilayer separated from the solid substrate by an ultrathin film of water (1-2 nm). [28] This thin aqueous layer confers to SLBs the fluidity required for lateral diffusion in 2D space [24], but restricts the incorporation of transmembrane proteins possessing extra-membrane domains [8,29–32], which are essential to their function. In tBLMs, the inner membrane leaflet is separated from the support by insertion of a soft and flexible hydrophilic layer of "tethering" molecules, which lifts the membrane off the surface and provides an aqueous reservoir underneath the bilayer in which the membrane proteins can fold into a native-like conformation, while keeping the membrane anchored (not supported) to the support. [28] This soft layer thus reduces the influence of the surface and the unfavorable frictions to the support. For this reason, tBLMs were used for membrane protein reconstitution [23,29,30,32–41]. They have been also used as screening platforms for biological [38,42–44] and biosensing applications. [39,42,44–48]

The different types of tBLMs mainly differ in the chemical structure of the tethers [15,17,20,29,31,32,44,49] and their tethering density, both factors significantly influencing the structural characteristics of the bilayer as well as the possibility to reincorporate functional transmembrane proteins [28,50]. Tethering molecules can be anchor lipids [45,51,52], polymers [23,31,37,39,53], peptides [29,54] or proteins [55–61]. Telechelics, anchor lipids coupled with polyethylene glycol (PEG), were the first to be used for tethering a lipid membrane [17]; however, for this important class of anchor lipids, neutron scattering [62] and PM-IRRAS studies [63] have revealed a poorly hydrated spacer segment, in spite of the water solubility of polyethylene glycol (PEG), due to the high tether density in the proximal leaflet.

Peptides have also been explored as tethering moieties to create peptide-tethered lipid bilayer membranes (pep-tBLMs). Among the different chemical classes of tethers used to form t-BLMs with the aim to improve space and hydration in the sub-membrane compartment, peptides offer the advantage to be actually of the same nature as the cytoskeleton inside or the extracellular matrix outside the cell with which the protuberance of the membrane proteins can interact in real life. [29] They are prepared from synthetic or native thiopeptides, or thiolipopeptides. [29] They are functionalized at their *N*-terminus by a sulfur group such as a cysteine or a lipoic acid so that they self-assemble from solution on gold - a surface of choice for biosensing applications -, whereas their C-terminus extremity is chemically activated afterward for coupling to the amino polar headgroup of various phosphatidylethanolamines (PE) in solution. These latter constitute the bilayer proximal leaflet. [44,54,64–66] The distal leaflet is formed in a second step by the fusion of liposomes possibly including proteins of interest onto the hydrophobic proximal layer. [32] Polar peptides used as tethers are suited for membrane protein reincorporation by providing a biocompatible sub-membrane environment in which extra-membranous subunits can fold with a native-like functional

conformation. Their length, their secondary structure, and their hydrophilic properties can be easily tuned by changing the aminoacid sequences to get a higher hydration level. This enables a flexible adjustment of both membrane–substrate separation and viscosity of the tethering units. [31] For these reasons, among tBLMs, pep-tBLMs are especially suited for membrane protein reconstitution. [67] Thus, numerous large integral membrane proteins have been successfully reincorporated in pep-tBLMs, e.g. cytochrome c [54], cytochrome bo_3 ubiquinol oxidases [68], H^+-ATPases [64,69], acetylcholine receptor dimer [66], integrins [70] or hERG potassium channels. [47] However, a proper reinsertion of a transmembrane proteins in the lipid bilayer is not a guarantee of a functional folding and only few reported on the functionality of the incorporated proteins. [36,45,68] Indeed, in the above-mentioned process, the two leaflets of the lipid membrane were formed independently, leading to protein misfolding. Recently, a new approach has been proposed to form the bilayer of the pep-tBLM in a single shot (see the Cartoon in Figure 1). [34,71] Preformed liposomes, including or not membrane proteins, were attached by a metal-chelate interaction to a natural thiopeptide spacer previously grafted on a gold substrate by a cysteine residue at its N-terminal extremity. [34] Then, the liposome fusion was triggered by an amphipathic α-helix (AH) peptide derived from the *N*-terminus of the hepatitis C virus NS5A protein to form pep-tBLMs. [72] This fusogenic peptide has been previously shown to induce bilayer formation on a gold substrate[73–76] and more recently, to form tBLMs on a polymer (PEG) cushion [39] or mesoporous silica[77]. The AH peptide binds to the vesicle surface, promotes vesicle swelling, and then desorbs, leading to the formation of a lipid bilayer.[78–80] The benefit of using peptides as tethers for entire vesicles is that the lipid composition of the vesicle membrane can be modified as desired and made more complex .[34] Hence, the membrane composition can be adapted to the membrane protein for its resinsertion in a native-like lipid environment. Additionnally, the attachment by chelation confers a great stability to the bilayer, when compared to the other pep-tBLMs described in the literature for which the attachment is ensured by hydrophobic interactions. These pep-tBLMs exhibit a smooth surface with a mean approximate height of 5 nm, the thickness expected for a pure phospholipid bilayer, and a diffusion coefficient of 2 - $2.5.10^{-7}$ cm²/s, consistent with those recently determined in complex membrane compositions.[81] By adapting the lipid composition, a C-X-C motif chemokine receptor 4 protein (CXCR4), a seven-transmembrane protein belonging to the large superfamily of G-protein-coupled receptors (GPCRs), was successfully reincorporated and its functionality checked by ligand binding assays after the pep-tBLM formation. [34,48]

The characterization and the use of tBLMs require highly sensitive surface techniques. The most frequently used are the label-free Surface Plasmon Resonance (SPR) [16,29,44,65,82] and Quartz Crystal Microbalance with Dissipation monitoring (QCM-D). [37,39] However, these techniques yield a global measurement, averaged over a large area, making it impossible to detect any material redistribution along the surface or to probe local mechanisms. Only imaging techniques allow to overcome these limitations. Among them, with a nanometer resolution in all directions, High-Speed Atomic Force Microscopy (HS-AFM) is unrivaled. A spectacular demonstration was given for instance with the dynamic study of the pore forming protein lysenin in a complex SLB membrane environment.[83] However, although progressively spreading, this technique remains very delicate to use, reserved to sharp specialists. For the study of tBLMs, the difficulty is even expected higher due to the fluctuating character of the tethered membrane. Besides, resolution is not everything and AFM suffers from a very limited field of view. In this context, with a simpler implementation, a lower resolution but an arbitrarily large field of view, enhanced contrast optical microscopies provide an interesting alternative. Among them, the most recent are Surface Enhanced Ellipsometric Contrast (SEEC) [84] and Backside Absorbing Layer Microscopy (BALM)[84,85]. As for the SPR, both techniques lie on the use of a special supporting plate providing background extinction in reflected light, hence high contrast of objects deposited on the plate. In the first one, this surface preserves the polarization state of the

incident light for a given non zero incidence and for all azimuth angles, so that extinction can be obtained between cross polarizers under a microscope. In the second one, which does not require a polarized light, the special surface is actually a window and extinction is insured in the backplane of the window by a novel type of antireflecting layer, named ARA (Anti-Reflecting and made of Absorbing materials).[86] The natural implementation of the SEEC is the upright polarization microscope, with observation of the sample from the top. The natural and only possible implementation of the BALM is the inverted geometry, with observation of the sample from the bottom. Both techniques may reach comparable sensitivities when used in their natural implementation. Although SEEC can also be used in the inverted geometry [87], it is generally less sensitive than BALM in this configuration by a factor 10 to 100 and it is more difficult to implement because of demanding constraints on the incidence angle [88] and because of the possible impact of the window on the polarization state of the light. Yet, SEEC has already been successfully implemented in the inverted geometry [89] and used to study biomimetic membranes [88]. In this particular configuration its use was limited to enhancing surfaces covered with silica but never with gold (which would require to work within a 65±5 deg. incidence), thus it could not be directly compared with SPR.

Here, we report the first application of Backside Absorbing Layer Microscopy (BALM) on a biological system to probe the forming process of a pep-tBLM that was previously characterized by SPRi, AFM and Fluorescence Recovery After Photobleaching FRAP. [34,48] BALM is a white-light wide-field optical microscopy. It combines SPR-like sensitivity with a 200 nm resolution[85]. On top of working *in situ* and in real-time, BALM is also simple to handle and flexible, because the top surface of the ARA coating can be almost any nature and observed in an ambient environment. The performance of the technique was already demonstrated by imaging 2D flakes of various materials, by following, *in situ* and in real-time, their evolution upon small molecules adsorption, [85] or by detecting operando the electrochemical reduction of individual sub-10 nm nanoparticles.[90] Recently, an universal relationship has been established between the BALM reflectivity and the physical thickness of a layer sample, ruled by three measurable quantities. [91] This relationship can be used without any knowledge of the microscope settings or the ARA coating in order to obtain a thickness map of the sample, whatever its (constant) complex refractive index, in a typical thickness range going from 0 to 30 nm. The thickness unit can be further determined with the help of a single reference measurement. The BALM reflectivity can also be averaged over the entire image, resulting in a global measurement similar to that of SPR or QCM-D. Here, we took advantage of these features to probe the transient structures arising during formation of pep-tBLMs, previsouly characterized by more classical methods, such as SPR, FRAP and AFM. [34] Except for the FRAP experiments which directly probe layer continuity, previous techniques could not provide any information on transient nanostructures. With BALM imaging, we were able to firstly reproduce the real-time quantitative measurements of the averaged deposited quantities previously obtained with the SPR, with a linear relationship between the two techniques for saturated quantities and secondly, to image, at the submicron level, the local material fluxes involved in each step of the process (*i.e.* tether peptide grafting, liposome attachement and liposome fusion).

In conjugation with the potential of tBLM as analytical tools, BALM live-watching of the formation and of the molecule-membrane interaction may bring answers to fundamental questions and open the field of numerous applications.

MATERIALS and METHODS

Reagents

HEPES and NaCl were purchased from Sigma-Aldrich (Saint-Quentin Fallavier, France). POPC (1-palmitoyl-2-oleoyl-*sn*-glycero-3-phosphocholine), DOPE (1,2-dioleoyl-sn-glycero-3-phosphoethanolamine), SM (sphingomyelin (brain porcine)), CHOL (cholesterol) and DOGS-NTA(Ni) (1,2-dioleoyl-*sn*-glycero-3-[(N-(5-amino-1-carboxypentyl)iminodiacetic acid)succinyl] Nickel salt) were purchased from Avanti Polar Lipids (Alabaster, AL, USA). Ultrapure water (18.2 MΩ.cm) was produced by PURELAB Option-Q (ELGA Lab Water, Veolia Water STI, Antony, France). Tether P19-4H (sequence: CSRARKQAASIKVAVSADRHHHH) and fusogenic AH (sequence: SGSWLRDVWDWICTVLTDFKTWLQSKLDYKD) peptides were synthesized by Smartox Biotechnologies (Saint-Egrève, France). All the reagents were of the highest analytical grade available.

Preparation of liposomes

Large Unilamellar Vesicles (LUVs) were prepared by thin film hydration with the compositions listed in Table 1. Briefly, lipids dissolved in chloroform were mixed in a round flask. The solvent was dried under vacuum at 50°C on a rotatory evaporator. The dry film was hydrated by 1 mL of HEPES 20 mM, NaCl 100 mM pH 7.4 buffer while stirring and heating at 70°C, resulting in the formation of MultiLamellar Vesicles (MLVs) with various sizes and layer numbers. Six freeze-thaw cycles in liquid nitrogen were then applied to the prepared liposomes in order to burst the MLVs into Large Unilamellar Vesicles (LUVs) as previsouly shown. [92]. The LUVs size was defined by extrusion through a 400 nm, then a 100 nm pore diameter polycarbonate membrane using a MiniExtruder apparatus (Avanti Polar Lipids), 21 times each. Dynamic light scattering (DLS) measurements of the size and polydispersity index (PDI) of the prepared liposomes were performed on a Malvern Zetasizer Nano ZS (Malvern Instruments S.A., Worcestershire, UK).

Table 1: Lipid compositions, mean size, and polydispersity indexes of the prepared liposomes.

Lipid composition	Molar percentages	Mean size (nm)	PDI
POPC/DOGS-NTA(Ni)	98:2	116.2 (± 0.4)	0.10
POPC/SM/DOPE/CHOL/DOGS-NTA(Ni)	42:35:10:11:2	123.5 (± 1.2)	0.12

pep-tBLM formation process

pep-tBLMs were formed in 3 steps. The first step corresponds to the grafting, to a gold surface, of a tether P19-4H peptide derived from the natural α-laminin thiopeptide P19 and widely used to form pep-tBLMs. [36,44,47,70] The grafting was insured by a natural cysteine residue at the peptide *N*-terminal extremity. The peptide used present four histidine residues in their C-terminal extremity, which allow the anchoring of liposomes doped with 2% molar ratio of a chelating lipid called DOGS-NTA. [34] In the presence of nickel, P19-4H and DOGS-NTA were able to bind. The liposome fusion was triggered by an α-helical (AH) peptide derived from the *N*-terminal extremity of the hepatitis C virus NS5A, originally used to induce bilayer formation on a gold substrate [73,76,78,93], as previously described. [34]

Surface Plasmon Resonance imaging (SPRi)

The pep-tBLM formation was monitored through a Horiba SPRi+ biosensor (Horiba Jobin Yvon SAS, Longjumeau, France). Glass prisms recovered by a thin 45 nm gold film and cleaned beforehand with ethanol were used to form the biomimetic membrane through the 3-step method previously described [34]. Briefly, a polytetrafluoroethylene (PTFE) holed cylinder was used to define a 400 µL

reaction chamber, filled with HEPES 20 mM, NaCl 100 mM pH 7.4 buffer. The PTFE cylinder was maintained against the gold-coated SPRi prism surface by means of a piston that holds the two against each other. A joint embedded in the PTFE cylinder's base assured the sealing of the reaction chamber. After stabilization of the signal, tether P19-4H peptides were added at a 10 µg/mL final concentration, then liposomes at 100 µg/mL and finally, fusogenic AH peptides at 200 µg/mL. Each injection was followed by a waiting time until the signal stabilization before rinsing. Rinsing was done by adding and then removing, 100 µL of fresh buffer to keep the reaction volume constant during the experiment. Repeating this operation 16 times ensured the removal of 99% of the excess sample material. The reflectivity changes were measured as a function of time. For each experiment, the typical curve shown was the average of curves obtained from the measurements of 16 different and independent 500 µm diameter zones defined on the SPRi prism.

Backside Absorbing Layer Microscopy (BALM)

BALM gold surfaces for immersed samples were obtained from Watch Live (Lyon, France) and placed on an Axiovert 25 inverted microscope equipped with a white light halogen source and a color AxioCam HRc camera and a x50/1.0 objective lens (Zeiss, Le Pecq, France). The same protocol as for the SPRi experiments was applied to the BALM gold substrates. Prior to BALM experiments, bare surfaces were cleaned in ethanol, the buffer was added on the support to adjust the focus, light intensity, aperture stop, and camera settings. The typical exposition was 300 ms for a 16 bits/12 Megapixels color image format.

Image analysis

Image analysis was performed using ImageJ. RGB images were split in three different images, each representing a different channel (either red, green or blue). BALM analysis was performed on the red channel signal, as it presents the largest variations. Images were colored using the inverted "phase" LookUp Table (LUT), which colors the low, medium and high intensities in red, white and blue, respectively. Plot was extended over a 1.2 µm line and were averaged over a 10-pixel width. Differential images were obtained in 32 bits format by subtracting two images one minute apart in the kinetics. From there, the FluxIn and FluxOut images were obtained by thresholding the positive and negative intensities, respectively. Composite images were formed by merging the past image and either the FluxIn or the FluxOut image in a same hyperstack.

RESULTS AND DISCUSSION

Pep-TBLM formation probed with BALM vs. SPRI

The formation of a pep-tBLM composed of 42% POPC, 35% sphingomyelin (SM), 10% DOPE, 11% cholesterol (given in mol%) was followed by SPRi and BALM in two parallel experiments. This composition closely resembles that of the plasma membrane. [94–97] The reflectivity signals obtained with SPRi and BALM are shown in Figure 1A. For the sake of comfortable comparison, the sign of the BALM reflectivity has been inverted. Indeed, we are in the case of a negative contrast, as will be explained further on. For clarity, we will name in the following the inverted signals Antired, Antigreen and Antiblue, and reserve the use of red, green and blue for the direct reflectivity.

The SPRi reflectivity was averaged over a cumulative area of 3.14 mm². The BALM reflectivity was split into three curves corresponding to the three color channels and averaged over the microscope image field, which makes a 0.013 mm^2 area. The acquisition frequency was also ten times faster with the SPR camera than with the BALM. By combining the two contributions, we would expect a 50 factor on the signal/noise ratio in favor of the SPR. It was found lower in this experiment, showing a BALM sensitivity at least comparable to that of SPR.

According to the cartoon in Figure 1, each step of the kinetics can be distinguished from either the SPRi or the BALM curve. After a first small variation induced by the tether peptide grafting, a large signal variation follows the liposome injection, indicative of liposome anchoring on tether peptides. After a brief further bump appearing right after the fusogenic peptide injection, indicative of liposome swelling, an opposite variation is observed, indicative of a matter loss as expected with liposome fusion. The correspondence between the reflectivities measured by the two techniques is very good, demonstrating the possibility of monitoring the adsorption/desorption phenomena using the BALM technique. It was equally confirmed on another system consisting of a pure POPC membrane (Supplements 1 and 2). Altogether, the qualitative SPR-BALM agreement is fully confirmed, but in order to support a quantitative comparison, a reminder of how the two measurements were interpreted is necessary. It is provided in the following paragraphs.

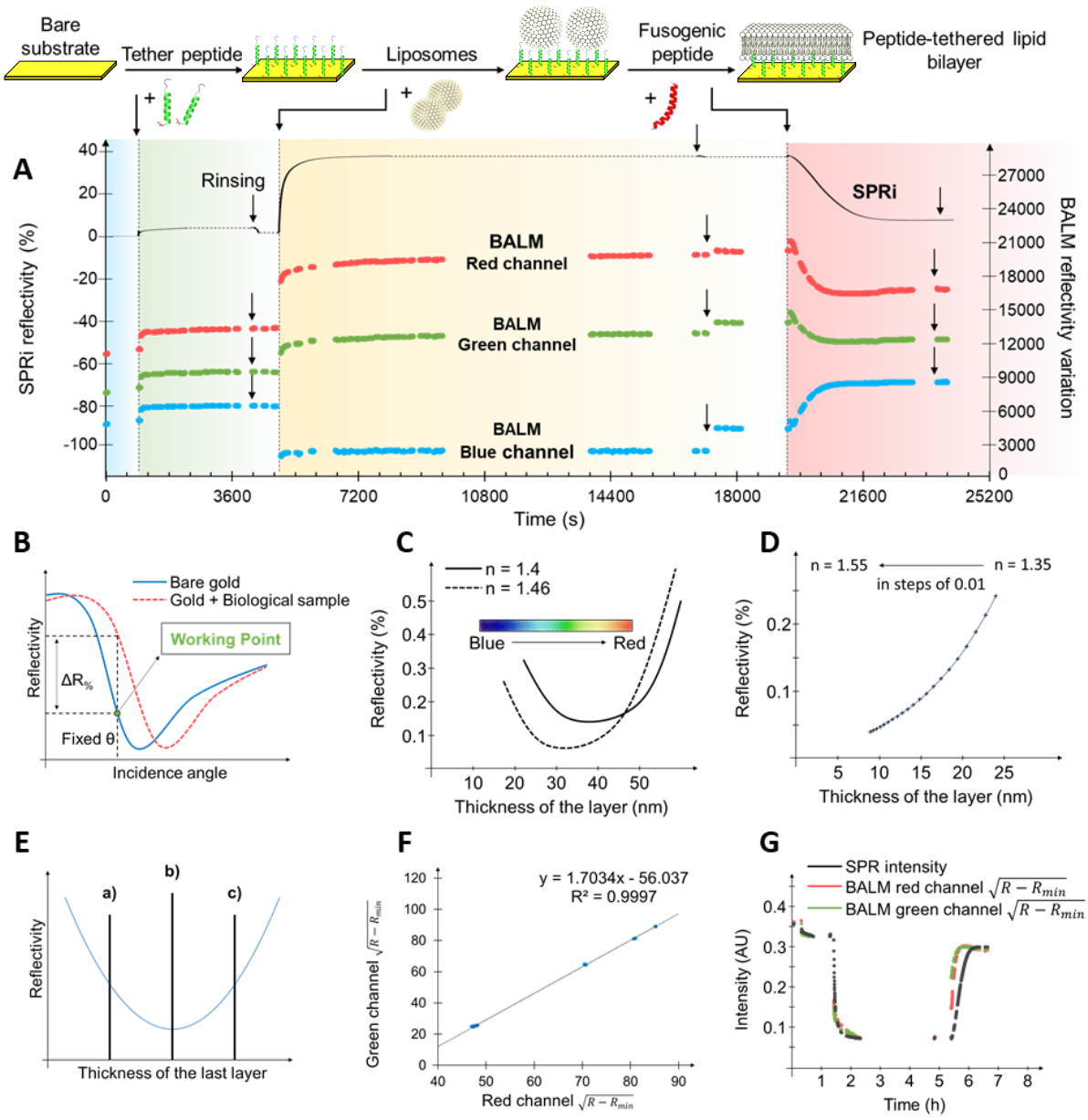

Figure 1: Comparison of SPRi and BALM reflectivities during the biomimetic pep-tBLM formation.

A. Evolution of the SPRi (black) and BALM reflectivities after inversion of the BALM curves (the colors correspond to the BALM channel). The SPRi reflectivity was counted from the SPR working point. The SPR reflectivity is given as the relative increase with respect to the reflectivity of the working point and the BALM reflectivity is given as the absolute intensity of the reflected image. For easier comparison, the origin of the vertical axis was independently adjusted for each curve.

B. SPR reflectivity as a function of incidence angle for the bare substrate (plain blue) or in the presence of a biological layer (dotted red). The presence of the probed layer generates a shift of the curve to the right, which results in a reflectivity change at a fixed incidence angle;

C. Numerical calculation of the (e_{min}, R_{min}) trajectory in the (e, R) plane for a 3 nm gold thickness, and a 30-degrees aperture angle, parametrized by the wavelength, for two fixed values of the layer refractive index.. The latter was taken pure (single wavelength) and continuously increasing from 400 nm on the left to 650 nm on the right.

D. Same as C, but with a single fixed wavelength of 480 nm and parametrized by the refractive index of the adsorbed layer, which is continuously increasing from 1.35 on the right to 1.55 on the left.
E. Schematic relationship between the BALM reflectivity and the probed layer thickness *e* counted from the substrate. The black line figures the relative positioning of the BALM parabola (multi-parameter dependent) and the thickness origin (bare substrate), which determines a situation of a) negative contrast, b) zero contrast or c) positive contrast.
F. Comparison of $\sqrt{R-R_{min}}$ for the red and green BALM channels, demonstrating a linear relationship between them. R_{min} was adjusted stage by stage using the entire in-stage measurements. Only the saturation levels (after rinsing) are kept in the figure.
G. Comparison of the SPRi signal with $\sqrt{R-R_{min}}$ for the BALM Red and Green channels after redistributing in y the SPRi intensities x *via* the affine transformation $y = ax + b$ with a = -1.35 and b = 80 for optimal fit with the BALM curve. Note that $|a|$ close to 1 demonstrates comparable sensitivity of the two techniques to layer thickness.

SPR Reflectivity vs layer thickness

SPR essentially probes a refractive index, namely the effective refractive index $\langle n \rangle$ of a volume slice with a depth Λ, which is of the order of 100 nm. Figure 1B shows a characteristic SPR reflectivity curve, with the angle of incidence in abscissa. Note that with BALM, the same curve on a similar angular range would be completely flat. Since imaging requires superposition of incidence angles, the low dependence of the BALM reflectivity on the incidence angle is actually the cornerstone of the BALM capability to combine sensitivity and imaging. In the most popular mode, SPR is used at a fixed incidence angle, which defines the working point. A great asset of SPR is the ease to make the exploited signal linear with the probed adsorbed quantity. When a layer with a thickness $e \ll \Lambda$ is added on the surface, $\langle n \rangle$ is perturbed by the local variation of n. The angular response shown in Figure 1B translates to the right according to the angular sensitivity to the average refractive index $\Delta\theta/\Delta\langle n \rangle$. The resulting change in reflectivity at the fixed working angle is also proportional to the local slope $\Delta R/\Delta\theta$ of the reflectivity curve. The overall SPRi sensitivity $S = \Delta R/\Delta\langle n \rangle$ is the product of the two quantities. It is estimated by a calibration procedure at the start of the experiment. The variation of ΔR with e is always monotonic with a choice of the working point on the left side of the minimum, as postulated in Figure 1B. It would go through a minimum with a choice on the right side. The (expected) linearity of ΔR with e, not only requires the linearity of ΔR with θ, but also the linearity of the lateral shift with e, or alternatively compensating non-linearities. To link ΔR and e, one should also connect $\Delta\langle n \rangle$ and e. Here comes a strong hypothesis, that the refractive index increment $\partial n/\partial c$ specific to the probed material is a constant. As a consequence, $\Delta\langle n \rangle = n(c) - n_0$, with n_0 the refractive index of the solvent, is locally proportional to the concentration c. Replacing c (g/mL) by $\rho\phi$, with ρ the (constant) density and ϕ the volume fraction of the probed material, Δn appears proportional to ϕ. The "strong" hypothesis is qualified strong because to apply it to the thin layer problem, it should cover the full range from $\phi = 0$ to $\phi = 1$. Then, we have $\Delta\langle n \rangle = (n_1 - n_0)\langle \phi \rangle$, with n_1 the refractive index of the pure layer material. For laterally homogeneous layers, $\langle \phi \rangle = \langle \phi \rangle_z$ is averaged over the volume probed by the SPR, *i.e.* over a thickness Λ. Only the part filled by the probed layer contributes, and we finally get:

$$\Delta R_{SPR} = \frac{\Delta R}{\Delta\langle n \rangle}\Delta\langle n \rangle = S(n_1 - n_0)\alpha\frac{e}{\Lambda} \quad (1)$$

where we added the surface coverage ratio α among the factors affecting the average. This equation is equivalent to the well-known Fleitjer's formula $\Gamma = (\Delta R/S)[\Lambda/(\partial n/\partial c)]$, with Γ the surface excess. It expresses the SPRi signal as the product of the probed layer differential refractive index, surface coverage, and thickness without possible separation of the three quantities, at least when

working with a single wavelength. When deriving Equation (1), we made another implicit approximation, which is uniform lighting in the Λ layer. If we account for the exponential decay in the evanescent wave and integrate over the accordingly weighted z volume elements, we find, instead of Equation (1):

$$\Delta R_{SPR} = \mathrm{S}(n_1 - n_0)\alpha\left(1 - e^{-\frac{e}{\Lambda}}\right) \quad (2)$$

Equation (2) shows the limits of the implicit approximation made in Equation (1). With e = 100 nm and Λ = 100 nm, for instance, as encountered with a liposome layer, the thickness estimated from Equation (1) is underestimated by 40 %. More information is given in Supplement 3. With SPRi in place of SPR, the same considerations apply down to the instrumental resolution. Here, we found helpful to derive Equations (1) and (2) from scratch by using the volume fraction instead of the more usual $\partial n/\partial c$, but similar results can be found for instance in References [98] or [99] with possibly a different meaning of Λ (depending if Λ is relative to the electromagnetic field or the energy) and S (defined by the sole factor $\Delta\theta/\Delta\langle n\rangle$ in [99].

BALM reflectivity vs layer thickness

BALM is an interferometric technique, which essentially probes the thickness e of a deposited layer on an ARA surface. The setup is schematized in Supplement 4. The BALM reflectivity $R(e)$ finds a real or virtual minimum (e_{min}, R_{min}) for a low value of $|e_{min}|$ because the thickness e_{gold} of the gold layer corresponds itself to a reflectivity minimum. In these conditions, it was shown that the BALM reflectivity obeys a parabolic variation with the thickness e of the added layer [91], (e_{min}, R_{min}) being the minimum of this parabola. The position and the amplitude of the parabola, hence the values of e_{min} and R_{min} are very sensitive to many factors, including the exact composition of the BALM substrate, the aperture of the microscope, the wavelength or the spectrum of the light source, the spectral response of the camera, and the refractive index of the solvent and of the added layer. For instance, based on numerical calculations, Figure 1C and 1D show the trajectory of the minimum (e_{min}, R_{min}) in the (e, R) plane for a 3 nm gold layer and a 30 degrees aperture when the refractive index of the probed layer and the wavelength of the source (supposed unique) respectively vary, the other parameter being kept constant. The key point is that the variation $R(e)$ remains parabolic whatever the detail of all the instrumental parameters. Based on this remark, the strategy proposed in [91] was therefore not to try to precisely handle all these parameters, but to determine case-by-case the three parameters which govern the exact shape of the parabola. As long as the refractive index of the added layer remains constant, knowledge of the three parameters is sufficient to convert the measured reflectivity into quantitative thickness measurements. The three parameters are e_{min}, R_{min} and the zero thickness (or bare substrate) reflectivity R_0. For a layer thickness tending towards zero, what we call "initial" state, the variation of the BALM reflectivity with e may be positive or negative, depending on the sign of e_{min}. The corresponding situations are referred to as "positive contrast" if $e_{min} < 0$, because the reflectivity will initially increase with the added layer and "negative contrast" if $e_{min} \geq 0$ because it will decrease. We insist that it refers to the *initial* contrast. The BALM parabola and the various contrast cases are illustrated in Figure 1E. With negative contrast, the reflectivity will decrease with increasing layer thickness until the minimum is reached and then increase with layer thickness. In the opposite case, $R(e)$ is a monotonically increasing function. In this case, the minimum of the parabola would be attained with a negative thickness, which is experimentally impossible, and the minimum is said virtual. Note that with SPR, choosing a working point on the right or the left side of the SPR curve (see Figure 1B) leads to similar negative and positive contrast situations. In Figure 1A, the variation of the red and green signals is monotonic and conforms to a case of negative contrast. In addition, the minimum of the red and green parabolas is never reached in the experiment because e is always lower than e_{min}. The blue

curve behaves differently. In Figure 1A, we cross the minimum during the second stage of the kinetics. As a consequence, the slope of $R(e)$ has an opposite sign in the first and the third stages. To simplify the analysis in the present work, the blue channel will be ignored. Since the green and the red channels both correspond to negative contrast, and since the green minimum is located on the left side of the red minimum, the red signal is always far from its minimum. In such conditions, the red signal is weakly non linear and closely ressembles the SPR signal. Following Abou Khachfe *et al*. [91], the BALM analysis lies on the fundamental equation:

$$f^2(R) \equiv \frac{R-R_{min}}{R_0-R_{min}} = \left(\frac{e}{e_{min}} - 1\right)^2 \quad (3)$$

To determine e/e_{min} from the measurement of R, we have to know the two parameters R_0 and R_{min}. The first one, R_0, is directly measured with the bare surface against the buffer solvent. The bare substrate can be chosen as the bare gold, making a global reference for the entire experiment, or else the gold already covered with a given component at the end of a given step (after rinsing) in order to focus the analysis of the next following step on the currently depositing layer. Note that the added layer has a different chemical nature in each stage of the kinetics presently investigated, thus a different refractive index. The second one, R_{min}, can also be directly obtained experimentally when the minimum is crossed during the experiment. It is not the case here with the red and green channels. Then, we may determine R_{min} from channel comparison. With the monotonic variation $R(e)$ with negative contrast as observed with the two channels, Equation (3) simplifies in $e/e_{min} = 1 - f(R)$, showing that $\sqrt{R - R_{min}}$ is a linear function of e, "linear" being taken in the sense of "affine". Therefore, $\sqrt{R_G - R_{min,G}}$ (for the green channel) and $\sqrt{R_R - R_{min,R}}$ (for the red channel) are also linear functions of each other (Figure 1F). This holds only with the two correct values of R_{min}. Thus, $R_{min,G}$ and $R_{min,R}$ can be obtained stage-by-stage by optimizing the two parameters such as to obtain a linear relationship between the two square root quantities. This process was implemented in Supplement 5. Note that R_0 , by contrast with R_{min}, does not affect this linearity, but only the slope of the straight line. Its value is not needed to build a function of R which is linear with thickness. The last unknown parameter in Equation (3) is e_{min}. It plays the role of the thickness unit and does not either affect the linearity of the relationship between e and $f(R)$. Its determination requires additional calibrating information. The e_{min} parameter in BALM is thus very similar to the S parameter in SPR, see Equation (1). About the thickness range for validity of Equation (3), the canonic BALM parabola is a low thickness approximation of a cosine variation as classically found with interferential methods. Considering that the cosine can be assimilated to a parabola from the minimum to the inflexion point, our analysis would be acceptable up to $n_1 e_{Max} = \lambda/4$ in the case of a negative contrast (while $n_1 e_{Max} < \lambda/8$ with a positive contrast). It typically gives 100 nm with $n_1 = 1.45$ for soft biological matter. [100] To summarize, the linearity of the SPR and the BALM reflectivities with layer thickness has a comparable validity range, slightly exceeded with the 120 nm liposomes in our experiment. Both techniques would underestimate such thickness.

From the present BALM experiment, one can read R_0 and obtain the values of R_{min} on each channel as explained above, but determining the e_{min} parameters (one per channel) requires additional information. A single correspondence between e and R is enough. For instance, we can find e_{min} with the help of one SPR measurement taken as an absolute reference. Then, provided that the two measurements are linked everywhere by a linear relationship, we would obviously obtain the same measured values with the BALM and with the SPR. However, our main concern is to demonstrate that SPR and averaged BALM deliver similar information. For this purpose, it is more direct to establish that the two quantities $f(R)$ and ΔR_{SPR} are linked all over the kinetics by a linear (affine) relationship with fixed coefficients. The existence of this linear relationship demonstrates interchangeability of the two techniques independently of any numerical value. In other words, interchangeability is insured by the existence of two coefficients a and b such as $f(R) = a *$

$\Delta R_{SPR} + b$, with R the BALM reflectivity. This existence is supported by Figure 1G for the entire kinetics and precisely demonstrated for saturation levels in Supplement 5.

Quantitative SPR estimation of the liposome coverage ratio

Quantitative estimations of the absolute peptide and bilayer thickness were already given for the same experimental system in [34] The main result was the thickness of the final bilayer, which value was estimated to be 5 nm. On the basis of Equation (1), Supplement 6 describes in details the expected evolution of ΔR_{SPR} during the three stages of the process, which should actually be decomposed in 7 steps to include the rinsing periods because of the refractive index change with each new solution. After injecting the values of the sensitivity S and of the penetration depth Λ relative to the present experiment, the difference between the after rinsing levels of the after fusion final layer (third stage) and of the tether layer (first stage) corresponds again to 5 nm. Here we will go one step further by comparing the after rinsing level of the three stages in order to estimate the coverage ratio of the surface by the two first components, which will prove to be as low as of order 50%. Because liposomes are made of a mixture of buffer and lipids, we suppose that only the lipids contribute to their refractive index. In Supplement 6, it is shown that the projected lipid layer (with lipid refractive index) equivalent to one liposome with diameter D has an effective thickness $6h$, with h the bilayer thickness, this layer being distributed on a disk with diameter D, the projected liposome footprint. Hence from different surface filling models one can estimate the average effective thickness of a liposome layer. The liposome layer after the second stage and rinsing is far from being saturated. Taking into account the liposome surface coverage α (see SPR Equations 1 and 2), the equivalent lipid thickness is $6\alpha h$. This is what we should measure if the SPR measurement of the large liposomes was not distorted. But we know from Equation (2) and Supplement 3 that the liposome surface excess, hence the equivalent lipid thickness is underestimated by the SPR measurement by a factor 1.59 due to the exponential relaxation of the evanescent wave. For comparison with other measured values, one must mimic this underestimation. The correcting factor to apply to the physical equivalent lipid thickness $6\alpha h$ in order to obtain the apparent SPR thickness [measured from Equation (1)] is therefore 1/1.59. We get $3.81\alpha h$. In simpler words, we expect $3.81\alpha h$ from the SPR measurement when the physical value is $6\alpha h$. This correction applies only to liposomes because of their large size. It does not apply to the after rinsing after fusion amount because at the end of the third stage, the layer is thin, most of the remaining liposomes being converted into flat lipid layers. The third stage level is 40 % of the second stage level, these levels including the first stage contribution, i.-e. the underlying thiopeptide layer. Taking into account this common contribution in the numerator and denominator of the 40% experimental ratio, we end up with a final lipid thickness 2.09 αh and we find $\alpha = 1/2.09 = 48\,\%$. A rigorous demonstration is given in the technical Supplement 6 after (re)deriving the equations used for the SPR analysis. The main approximation made was to replace the liposome refractive index distribution by its average over the liposome thickness in order to derive its contribution to the SPR signal.

Concerning at last the tether peptide layer, one can estimate from Figures 1F or 1G that the tether peptide saturation signal is typically half of the final bilayer saturation signal (to which it is added at the end of the experiment). Using this value, taking $n_0 = 1.34$ for the solution, $n_1 = 1.50$ and $e_1 = 5nm$ for the bilayer and $n_1 = 1.42$ for the peptide layer because it is much more hydrated, reporting these values into Equation (1) (or Equation S11-11), and comparing tether and lipid terms, we get αe_1 of order 5 nm for the tether peptide. Since the extended peptide is 9 nm long and the globular peptide less than 3 nm in diameter, this is perfectly consistent with a dense peptide layer covering a minority fraction of the surface, namely 1/3 with these numbers, and with a low peptide density elsewhere.

At least, one should mention that our analysis of the SPR signal, which consists in the incoherent summation of all the refractive index contributions in the evanescent wave, ignores interferential contributions related to refractive index structuration in the lighted film. Such contributions are expected with the two lipid peaks corresponding to the top and bottom of the liposomes spheres. Expressing the corresponding corrections would require a higher level model. In the present work, we stay at the level of analysis which is implemented on commercial SPR instruments and practiced by a large majority of SPR users.

The aim of the present study is to probe the mechanisms involved in the tethered bilayer formation. As they involve inhomogeneities and matter exchange at a local scale, the information extracted from global measurements is very limited. Focusing on averaged quantities over the surface could even have the pernicious effect to encourage to view the surface as invariant and to interpret the results as if the surface was evolving in a uniform way, according to closely packed and repeated dynamic patterns. To our knowledge, this is how the results were interpreted in all previous investigations. In order to probe local mechanisms, we must overcome surface integrated measurements. This is made possible by the BALM imaging capabilities. We shall also see that the direct local observations give a stronger evidence of the presence of a final regular bilayer than any surface-averaged measurement, subjected to several assumptions, approximations and interpretations.

Imaging the local topography during pep-tBLM formation

With SPRi, lateral resolution is intrinsically limited to around 20 microns by the extension of the propagating surface plasmons. By contrast, BALM in this experiment has the diffraction-limited resolution of optical microscopy, *i.e.* 200 nm, approaching the 120 nm liposome diameter. The two resolutions differ by two orders of magnitude. With better-resolved images, we can locally follow the sequential reactions on the surface. BALM imaging contributions are illustrated in Figure 2A, where typical snapshots of the same (7 x 5) µm² zone of the sample were extracted from the kinetics and associated with the corresponding point of the averaged red BALM curve. The ten “antired” images of the series are displayed with the same Look Up Table (LUT), with blue and red colors extending below and above the white average level, respectively. The minimum and maximum intensity levels in the LUT, hence the LUT range, are the same in all images, making meaningful color comparisons in the series. The global color evolution of the BALM images conforms with the BALM reflectivity curves, with a blue or red dominance depending on the intensity of the Anti-BALM signal. Note the apparition of a white pattern (hence higher thickness) on the buffer blue background with tether peptide injection (Figure 2A, 2 and 3) and the strong shift from blue to white and from white to red (hence further higher thickness) with liposome injection (Figure 2A, 4 to 6). Finally, the fusogenic peptide injection makes the layer thickness increase in a first time (Figure 2A, 7), before gradually decreasing as indicated by the shift to bluer and whiter hues (Figure 2A, 8 to 10), to reach a final situation consistent with a lipid bilayer grafted on top of the tether peptides. This evolution is also visualized in a topographic mode with the surface plots shown in Figure 2B, highlithing strong correlations in the images of a same 1µm² area in the buffer stage (1), the end of each step after rinsing (2, 3 and 5) and the very beginning of the fusion stage (4).

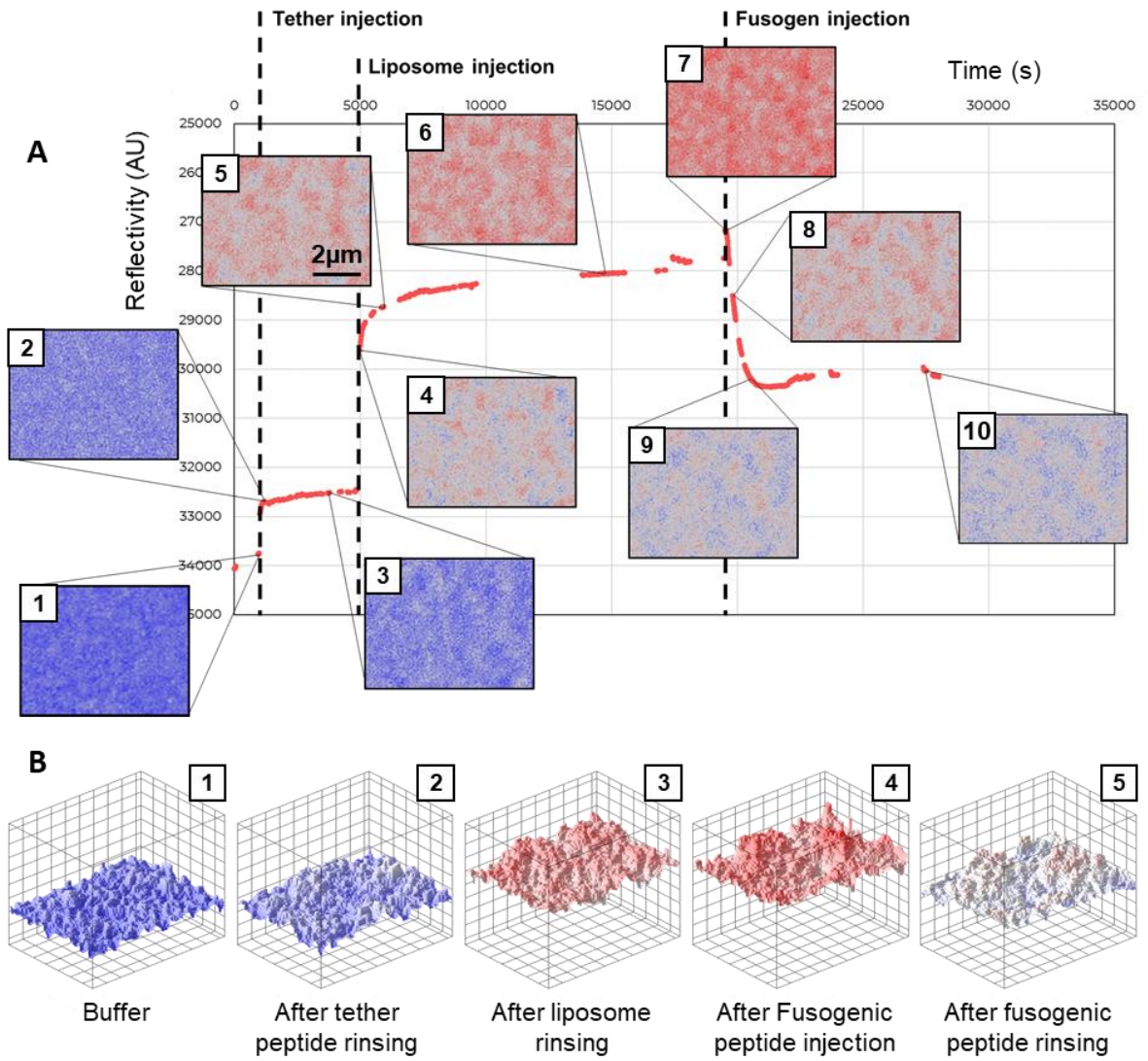

Figure 2**:** Local evolution of the sample at the submicron scale during the formation kinetics of the biomimetic pep-tBLM. A similar representation for a POPC membrane is shown in Supplement 7.
A. Series of high resolution images each associated with the corresponding point in the AntiBALM curve.
B. Surface plots showing the local evolution of the surface patterns for significant steps in the formation process over a 0.9µm x 1.2µm area.

The most striking characteristic of these images is the presence of a persistent pattern, from the second image onwards. They appear with the tether peptide injection (Figure 2A, 2) and show a clear correlation with a pre-existing pattern in the buffer solution (Figure 2A, 1). A point of importance is that prior to peptide injection this pre-existing pattern was constantly renewing with no correlation at all between consecutive images taken one second apart. This fluctuating pattern cannot be attributed to any constitutive irregularity or pollution of the gold surface. It is necessarily due to some component in the buffer solution. The correlation of the last observed pattern before peptide injection and the same reinforced pattern observed after peptide injection shows that the adsorption of the tether peptide is guided by the distribution of the said component. Once this early adsorption occurred, the resulting pattern will last for the entire experiment. This observation makes also BALM appear as a powerful tool to probe local surface chemistry, including catalytical mechanisms.

The persistent pattern may hamper the detection of the deposited material during each further stage. This is why a refined analysis requires either to follow the quantitative evolution of these patterns during the kinetics, as done along a line in Figure 3, or to use differential images in order to highlight the molecular fluxes, as done in Figure 4.

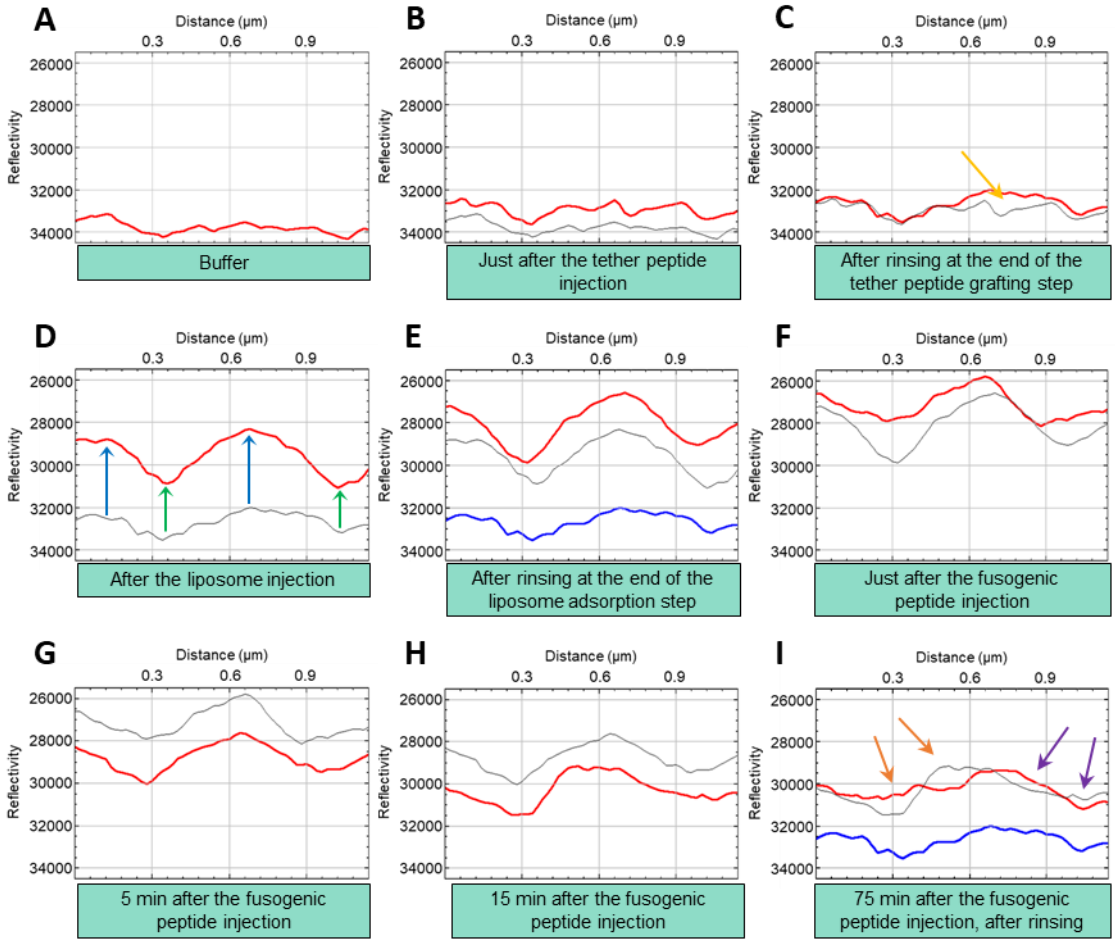

Figure 3**:** Direct plot profiles of the BALM red channel with inverted intensity scale along a ten-pixel wide, 1.2 µm long line at nine significant steps of the peptide-tethered bilayer formation from biomimetic liposomes. In red, the plot profile corresponding to the given step; recalled in grey, the plot profile of the previous step; recalled in blue (Figure 3E and I) the plot profile corresponding to the end of the tether grafting step. Each plot profile was obtained after averaging the signal of four successive images, applying both an inverted phase LUT and a median 1-pixel wide filter. The images used are available in Supplement 8. Similar measurements for a POPC membrane are available on Supplements 9 and 10.

Figure 3 shows the evolution of a same surface profile at nine significant stages of the kinetics, indicated in the figure. Figure 3A shows the pattern which was pre-existing before tether peptide injection. It is recalled in grey in Figure 3B, and juxtaposed with the new profile, in red, immediately following the peptide injection. We have proceeded in the same way in all further sub-figures. Adsorption of the tether peptides is clearly guided by the buffer pattern. Figure 3C shows tether peptide aggregation with formation of enlarging plateaus, as pointed by the yellow arrow. Once formed, these growing aggregates will keep a constant height, which proves the absence of vertically growing structures. It suggests a conformational change of the peptide molecules from either globular or horizontal at low density to vertical and closely packed at high density, as classically

found with self-assembled monolayers. The coverage ratio at the end of the tether grafting stage is ill-defined because of the coexistence of these different peptide density states. Most of the surface is covered, but only part of it is covered by the dense plateau.
Figures 3D and 3E show that the tether surface pattern is further reinforced by the liposome deposition, showing a preferential interaction with peptide-rich (blue arrows) compared to peptide-poor regions (green arrows). At the end of the liposome grafting step, the whole surface is covered with lipid material, although the total layer thickness is not homogeneous. Considering that the tether acts as an anchor for the liposomes, it makes sense that peptide-rich regions attract more liposomes than peptide-poor ones.
The remaining plot profiles, Figures 3F to 3I, illustrate the reputed most critical stage, the liposome fusion. The first one shows an initial increase in layer thickness which is consistent with previous QCM-D experiments on forming SLBs.[76] It was shown that the fusogenic peptide was inserting in a curved membrane like the one of liposomes, causing the formation of pores and/or microvilli in the membrane, then swelling of the liposomes by the buffer before liposome rupture after a small delay. [76,93] Figure 3F shows that the early fusogenic peptide action was concentrated in the regions with the lower lipid density. From there, one may infer that the liposomes in the lower density regions are more flat, thus exhibiting a higher curvature at their edge. Indeed, it was shown that the insertion of the fusogenic peptide is favored by the presence of a high membrane curvature. [101] The profile obtained at the end of this stage, displayed in red in Figure 3I, is very similar to that in Figure 3C, recalled in blue. It demonstrates a uniform thickness shift with respect to the tether pattern, which is perfectly consistent with the presence of a regular bilayer. The arrows in Figure 3I point the late stage lateral flows which had to take place between Figures 3H and 3I to reach this situation. These rearrangements clearly respect matter conservation at the micron scale. They can be as well directed up (purple arrows) or down (orange arrows) the tether density gradient, with the global effect of smoothing the deposited material to reach a uniform bilayer. Moreover, the existence of these surface fluxes even after fusogenic peptide rinsing demonstrates by itself bilayer continuity. Concerning the fusogenic peptide, it was demonstrated with SLBs that the fusogenic peptide desorbs from the lipid membrane when its curvature disappears, so it should not remain present in the planar bilayer. [73,76]

To gain further insights into the local dynamics, differential images were used to point the FluxIN and the FluxOUT happenings, *i.e.* the added and departed matter, respectively. The FluxIN and FluxOUT images were obtained after substraction of an image to another image taken one minute further, with FluxIN images colored using the “Yellow” LUT, and FluxOUT using the “Green” LUT. Then, they were superimposed to the first image displayed with the phase LUT (red for high density and blue for low density). Figure 4 presents sets of original, FluxIN and FluxOUT images at many instants of the kinetics.
Figures 4A and 4B address the tether peptide grafting step. Comparison of the FluxIN and FluxOUT images shows that the yellow area is much greater than the blue, showing that peptide adsorption from the solution is more important than desorption or lateral displacement. Figures 4A and 4B show that grafting starts on the pre-existing pattern and then takes place at the edge of the aggregates, consistent with their observed height saturation. The existence of the minority blue spots in the regions with intermediate density (white) reveals either desorption or migration of the low density peptides. Because the amount of blue is higher at the beginning of the stage than after (line A vs line B), it cannot be desorption towards the solution. Indeed, desorption would not decrease with increasing adsorbed amount. It demonstrates lateral mobility of the “grafted” peptide molecules from the low-density towards the high-density regions. Similar mobility of grafted alkyl-thiols was previously reported. [102] To summarize, peptide adsorption proceeds from nucleation and growth,

with a twofold growth mechanism (adsorption and migration), while nucleation is triggered by the pre-existing buffer pattern.

The next set of images, Figures 4C and 4D, shows that the liposome adsorption takes place in the regions with high peptide density, in agreement with previous Figure 3D. It is therefore dependent either on the density or the conformation of the adsorbed peptides. An important observation is that the FluxOUT is absent from the beginning of the liposome stage and present at the end, mainly located in the low density regions. With the same argument as before, it cannot be desorption. We incline for short range liposome migration to reinforce aggregates, because of the remarkable balance between the yellow and the blue areas. In other words, the lipid material climbs the sides of the aggregates. To explain the absence of FluxOUT in Figure 4C, we would infer very different kinetic constants in the high and low density regions.

Figures 4E-4J were taken during the fusion stage. Figure 4E shows that in the first minute of the fusion stage, the fusogenic peptide invades the aggregated liposomes. It seems in contradiction with figure 3F where the fusogenic peptide was seen to privilege the spread liposomes. But this is just a question of a different time scale. Indeed, five minutes later (Figure 4F), a dominant material loss is observed, which takes place essentially in the white regions with lower intermediate thicknesses. It must follow a matter fusogenic FluxIN between one and five minutes in the same regions, which was missed in Figure 4. Comparison of the raw images in the two figures actually reveals the spreading of large white, intermediate-density zones around the red aggregates within the five minutes time interval. The next Figures, 4F and 4H present common trends, with a dominant fluxOUT located in the intermediate-density zones, and a weaker fluxIN mainly located in the pink regions juxtaposing the red ones. Hence, the intermediate thickness is fed on one side by the liposomes in fusion, and drained on the other side by the lipid escaping towards the solution. Altogether, the white zone supports important lipid fluxes. The IN and OUT surface fluxes in the white layer cannot be balanced at any time, and we actually see that the white layer area is reduced between 4F and 4G before increasing again in 4H and 4I. These fast and fluctuating exchanges between the white layer and the remaining liposomes resemble the respiratory swelling of a hydrophilic layer in a humid atmosphere. They are the mark of a continuous lipid layer, which progressively percolates over the surface. Figure 4I and 4J show that the lipid rearrangement on the surface goes on at constant lipid quantity (shown by identical yellow and blue surface coverages) for hours. The persistence of the balanced FluxIN and FluxOUT late after rinsing demonstrates that these fluxes are actually surface flows. It requires the presence of a fluid membrane covering the surface. These results are consistent with those previously obtained in Figure 3I, which showed that the coverage over the initial peptide pattern is uniform at the end.

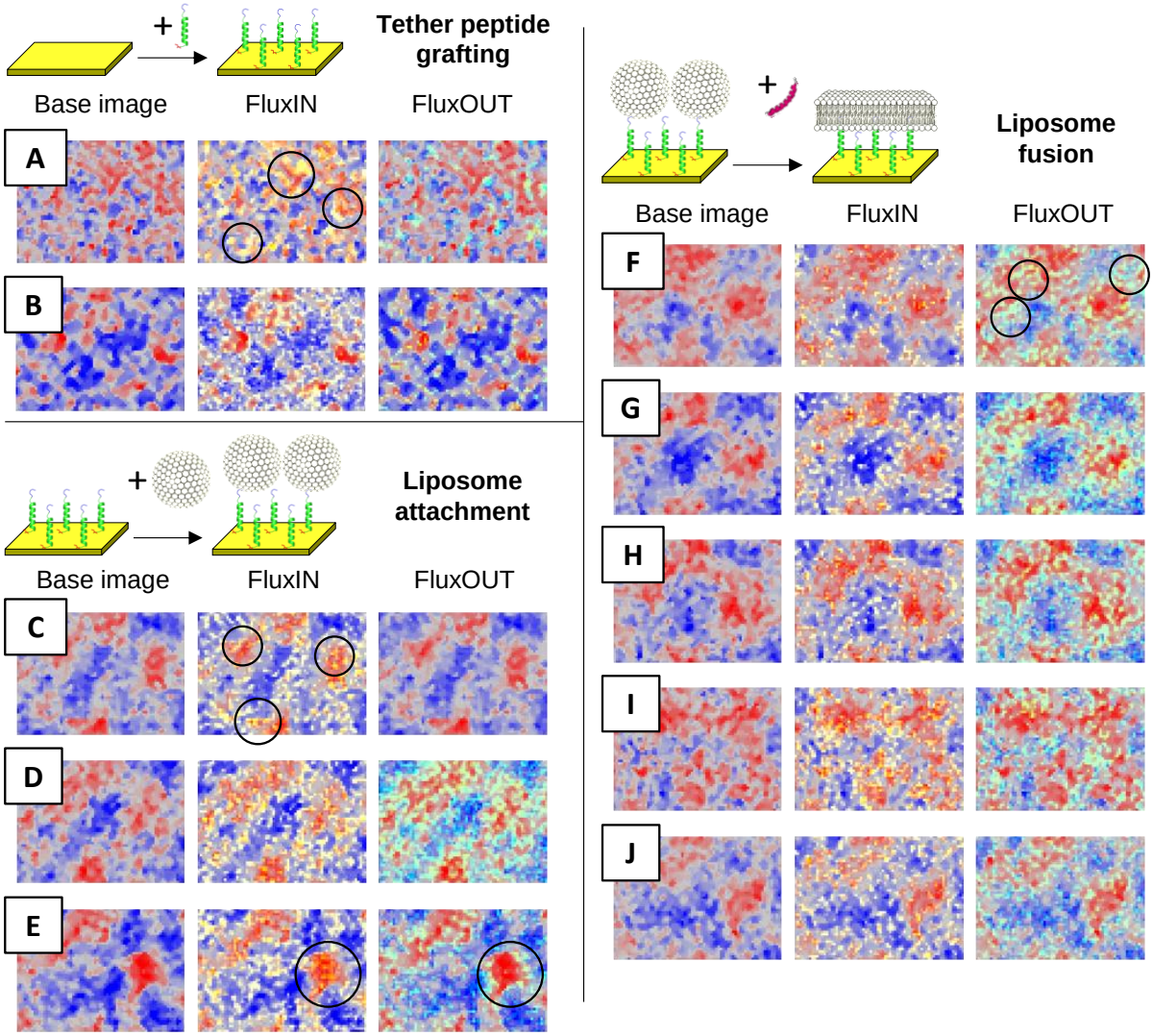

Figure 4: Eight series of 14 µm x 10 µm images (left) repeated with superimposed FluxIN (middle) and FluxOUT (right) differential images. The raw images were corrected by substracting the first image of the corresponding stage, which does not affect the FluxIN and FluxOUT images. The resulting images were colored with the "phase" LUT, with FluxIN in yellow and FluxOUT in green. Contrast in each raw image was adjusted independently to maximize the height difference, and a median 1-pixel wide filter was applied to help the eye focus on the lateral patterns. Hence, color comparison between any couple of images does not give any information on local thickness evolution. It only helps to locate the FluxIN and FluxOUT contributions with respect to the persistent pattern. FluxIN and FluxOUT represent the evolution of the image intensities over 1 minute. A. just after the tether peptide injection; B. 10 minutes after tether peptide injection; C. just after the liposome injection; D. 15 minutes after the liposome injection; E. just after the fusogenic peptide injection; F. 5 minutes after the fusogenic peptide injection; G. 15 minutes after the fusogenic peptide injection; H. 30 minutes after the fusogenic peptide injection; I. 1h after the fusogenic peptide injection; J. 2h after the fusogenic peptide injection and rinsing.

Up to now, it was considered that the rupture of the liposomes was immediately yielding a flat membrane, with the fusogenic peptide escaping after this transformation [76,79]. This experiment

confirms that the fusogenic peptide converts the large liposomes into thinner structures, but not immediately into a large uniform bilayer spread all over the surface. From the above description, the transient nano-structures are rather finite extend bi- or transitory multilayers continuously exchanging with liposomes and progressively percolating to eventually form flat membranes. A schematic drawing is proposed in Figure 5A**,** where such late liposome remnants coexist as vesicular pockets with the bilayer, sharing one wall with it and free to move by rolling over it. This view would be consistent with the displacements observed after rinsing in Figure 4J. It must be stressed that those pockets occupy only a small fraction of the surface layer. The final layer is therefore mostly regular and continuous, in agreement with the conclusions of previous AFM and FRAP studies.[34]
Finally, Figures 5B and 5C demonstrate with an example taken in the liposome binding stage that BALM offers the possibility to conduct very local kinetic studies. They show the evolution of two spots with respectively a high and a low tether density. The area of the former is 0.4 µm² and that of the latter 0.2 µm². This is thousand times smaller than the SPRi measuring resolution 400 µm². The comparison of the two curves supports the conjecture of lipid mobility from low to high density regions. The spots used are shown in Supplement 11, together with similar local kinetics in the tether and the fusion stages.

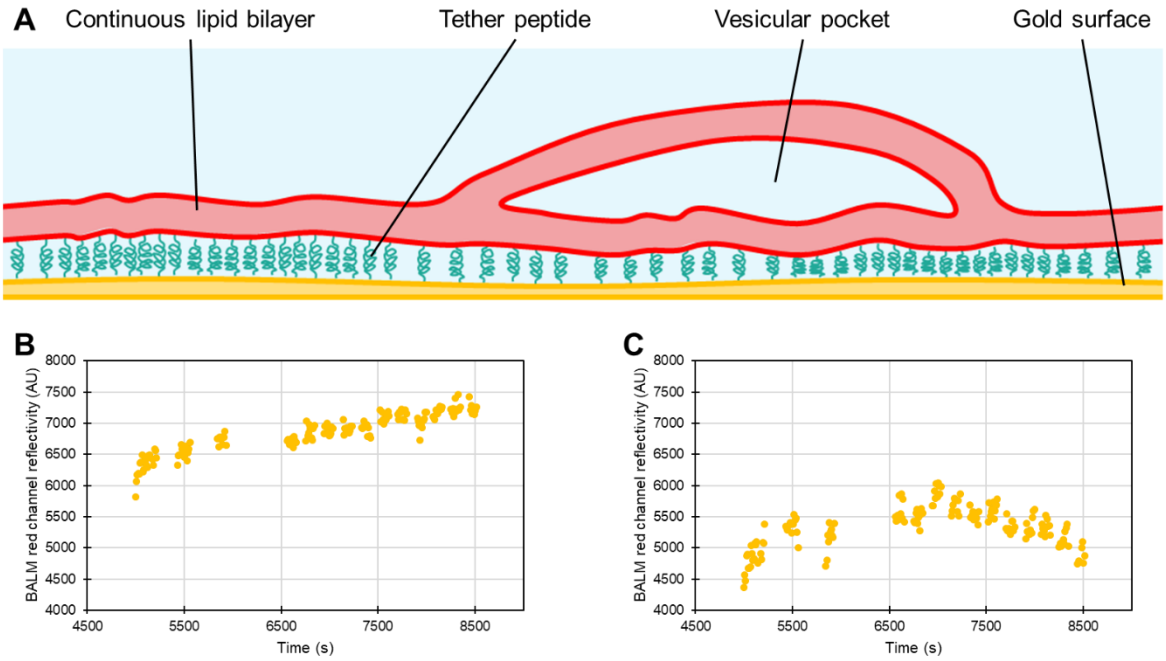

Figure 5: Local structural insights and measurements enabled by BALM.
A. Schematic drawing of the proposed surface lipid structure at the end of the fusion step with realistic scales. B. Local kinetics of the liposome grafting stage over an 0.4 µm² spot with a high tether density. C. Same kinetics over an 0.2 µm² spot with a low tether density.

CONCLUSION

To conclude, when using BALM to monitor the formation of biomimetic peptide-tBLMs, the SPR results are quantitatively reproduced by the averaged intensity of the BALM images after appropriate transformation, with an exact correspondence of the saturation levels, and a correspondence comparable to the SPR reproducibility for the entire kinetics. This transformation renders the BALM response linear (with thickness) and allows a self-calibration of the BALM signals without any

knowledge of the instrumental parameters, based on the comparison of two color channels. This is promising for automated procedures. It is worth to mention that the same signal processing could extend as well to other sensitive techniques such as SEEC or even SPR itself.

Yet, beside reproducing the surface averaged measurements which were already available with SPR and confirming the expected final formation of a (majority) regular bilayer, the main contribution of the BALM technique is to improve the resolution of these measurements by two orders of magnitude, giving access to local phenomena. In the present study, it made us discover the presence of unexpected heterogeities on a surface sample that up to now had ever been considered smooth. Thanks to this resolution, the implication of some buffer component in the peptide grafing or the nucleation-growth mechanism involved in the peptide layer formation was also demonstrated. One should not be surprised by sample heterogeneity since heterogeneous deposition is inherent to this mechanism. The other important features that were evidenced are the after-grafting peptide mobility, the presence of highly mobile and fluctuating liposome remnants decorating the final bilayer, the persistence of the initial peptide pattern governing every subsequent matter adsorption and desorption until the end of the process, and the correlation between the shape of the liposomes and the time scale of the fusogenic peptide insertion in their membrane.
Beside confirmation of previous studies and complementary information, this work demonstrates, under the control of the reference technique SPRi, the application of BALM to very local (sub-µm²), real time and quantitative studies of in biomolecular processes and surface chemistry. Considering similar implementation, similar measuring capacity and much higher imaging possibilities, BALM should rapidly rise alongside SPR in daily biological, pharmaceutical and medical research. With a great simplicity in the instrumentation, it should also constitute an effective basis for the development of ultra-high density and low-cost imaging sensors. In conjugation with the potential of tBLMs as analytical tools, BALM live-watching of molecule-membrane interactions should shortly bring answers to fundamental questions and serve numerous applications.

ASSOCIATED CONTENT

Supporting Information.

A listing of the contents of each file supplied as Supporting Information should be included.
brief description (file type, i.e., PDF)
All supplements are grouped in a single pdf file entitled “Supplements”.
Supplement 1: The analog of Figure1 obtained with the POPC model system.
Supplement 2: Third (fusion) stage kinetics as seen with BALM and SPR with the POPC system.
Supplement 3: The limits of SPR linearity with thickness. The field profile in the evanescent wave is taken into account in order to derive the correction factor to apply to thick probed layers.
Supplement 4: Principle of the BALM measurement and schematic setup.
Supplement 5: Quantitative comparisons. First it is explained how the values of the BALM R_{min} parameters (one per colour), hence the BALM f(R) transformations, are found from BALM color comparisons. Second, it is shown that linearized BALM and SPR signals are qualitatively the same. Third the reproducibility of the two techniques in a multispot measurement are compared. Fourth the measured BALM and SPR saturation levels are quantatively compared.
Supplement 6: Stage by stage analysis of the SPR signal; conversion of the liposomes into equivalent lipid films; derivation of the after rinsing liposome surface coverage.
Supplement 7: Local evolution of the sample at the submicron scale during the formation kinetics of the POPC pep-tBLM.
Supplement 8: Images used to make the plot profiles in Figure 3.

Supplement 9: Plot profiles along a ten-pixel wide, 1.2 µm long line at nine significant steps of the peptide-tethered bilayer formation from POPC liposomes (analog to Figure 3 from Biomimetic liposomes).
Supplement 10: Images used to make the plot profiles in Supplement 8.
Supplement 11: Local (submicron) kinetic measurements in the liposome stage (Biomimetic system).

AUTHOR CONTRIBUTIONS

JB conducted experiments; JB, OM and DA analyzed the data; RA and DA contributed analytic tools; JB and DA developed the analytical model based on underlying physical parameters; AGE and DA designed research; AGE supervised the work; JB, DA and AGE wrote the manuscript.

ACKNOWLEDGMENTS

Julien Bompard was supported by a French Ministry of Higher Education and Research fellowship. We would like to thank Dr Giovanna Lollo for her help in DLS measurements performed at LAGEPP UMR 5007, CNRS/University of Lyon, France. This work was supported in parts by CNRS and University of Lyon 1.

REFERENCES

(1) van Meer, G.; Voelker, D. R.; Feigenson, G. W. Membrane Lipids: Where They Are and How They Behave. *Nat Rev Mol Cell Biol* **2008**, *9* (2), 112–124.
(2) Nicolson, G. L. The Fluid-Mosaic Model of Membrane Structure: Still Relevant to Understanding the Structure , Function and Dynamics of Biological Membranes after More than 40 Years. *Biochim Biophys Acta* **2014**, *1838* (6), 1451–1466.
(3) Yin, H.; Flynn, A. D. Drugging Membrane Protein Interactions. *Annu Rev Biomed Eng* **2016**, *18*, 51–76.
(4) Tamm, L. K.; McConnell, H. M. Supported Phospholipid Bilayers. *Biophys. J.* **1985**, *47* (1), 105–113. https://doi.org/10.1016/S0006-3495(85)83882-0.
(5) Brian, A. A.; McConnell, H. M. Allogeneic Stimulation of Cytotoxic T Cells by Supported Planar Membrane. *Proc Natl Acad Sci USA* **1984**, *81* (19), 6159–6163.
(6) Sackmann, E. Supported Membranes: Scientific and Practical Applications. *Science (80-.).* **1996**, *271* (5245), 43–48. https://doi.org/10.1126/science.271.5245.43.
(7) Sackmann, E.; Tanaka, M. Supported Membranes on Soft Polymer Cushions: Fabrication, Characterization and Applications. *Trends Biotechnol.* **2000**, *18* (2), 58–64. https://doi.org/10.1016/S0167-7799(99)01412-2.
(8) Wagner, M. L.; Tamm, L. K. Tethered Polymer-Supported Planar Lipid Bilayers for Reconstitution of Integral Membrane Proteins: SilanePolyethyleneglycol-Lipid as a Cushion and Covalent Linker. *Biophys J* **2000**, *79* (3), 1400–1414.
(9) Cullison, J. K.; Hawkridge, F. M.; Nakashima, N.; Yoshikawa, S. A Study of Cytochrome c Oxidase in Lipid Bilayer Membranes on Electrode Surfaces. *Langmuir* **1994**, *10* (3), 877–882.
(10) Terrettaz, S.; Mayer, M.; Vogel, H. Highly Electrically Insulating Tethered Lipid Bilayers for Probing the Function of Ion Channel Proteins. *Langmuir* **2003**, *19* (14), 5567–5569.
(11) Silin, V. I.; Wieder, H.; Woodward, J. T.; Valincius, G.; Offenhausser, A.; Plant, A. L. The Role of Surface Free Energy on the Formation of Hybrid Bilayer Membranes. *J Am Chem Soc* **2002**, *124* (49), 14676–14683.
(12) Ogier, S. D.; Bushby, R. J.; Cheng, Y.; Evans, S. D.; Evans, S. W.; Jenkins, A. T. A.; Knowles, P. F.;

Miles, R. E. Suspended Planar Phospholipid Bilayers on Micromachined Supports. *Langmuir* **2000**, *16* (13), 5696–5701.
(13) Römer, W.; Steinem, C. Impedance Analysis and Single-Channel Recordings on Nano-Black Lipid Membranes Based on Porous Alumina. *Biophys J* **2004**, *86* (2), 955–965.
(14) Römer, W.; Lam, Y. H.; Fischer, D.; Watts, A.; Fischer, W. B.; Göring, P.; Wehrspohn, R. B.; Gösele, U.; Steinem, C. Channel Activity of a Viral Transmembrane Peptide in Micro-BLMs: Vpu1−32 from HIV-1. *J Am Chem Soc* **2004**, *126* (49), 16267–16274.
(15) Guidelli, R.; Aloisi, G.; Becucci, L.; Dolfi, A.; Rosa Moncelli, M.; Tadini Buoninsegni, F. Bioelectrochemistry at Metal/Water Interfaces. *J Electroanal Chem* **2001**, *504* (1), 1–28.
(16) Naumann, R.; Schiller, S. M.; Giess, F.; Grohe, B.; Hartman, K. B.; Kärcher, L.; Köper, I.; Lübben, J.; Vasilev, K.; Knoll, W. Tethered Lipid Bilayers on Ultraflat Gold Surfaces. *Langmuir* **2003**, *19* (13), 5435–5443.
(17) Lang, H.; Duschl, C.; Vogel, H. A New Class of Thiolipids for the Attachment of Lipid Bilayers on Gold Surfaces. *Langmuir* **1994**, *10* (1), 197–210.
(18) Schilleer, S. M.; Naumann, R.; Lovejoy, K.; Kunz, H.; Knoll, W. Archaea Analogue Thiolipids for Tethered Bilayer Lipid Membranes on Ultrasmooth Gold Surfaces. *Angew Chem Int Ed* **2003**, *42* (2), 208–211.
(19) Förtig, A.; Jordan, R.; Graf, K.; Schiavon, G.; Purrucker, O.; Tanaka, M. Solid-Supported Biomimetic Membranes with Tailored Lipopolymer Tethers. *Macromol Symp* **2004**, *210* (1), 329–338.
(20) Knoll, W.; frank, C. W.; Heibel, C.; Naumann, R.; Offenhäusser, A.; Rühe, J.; Schmidt, E. K.; Shen, W. W.; Sinner, A. Functional Tethered Lipid Bilayers. *Rev Mol Biotechnol* **2000**, *74* (3), 137–158.
(21) Rossi, C.; Homand, J.; Bauche, C.; Hamdi, H.; Ladant, D.; Chopineau, J. Differential Mechanisms for Calcium-Dependent Protein/Membrane Association as Evidenced from SPR-Binding Studies on Supported Biomimetic Membranes. *Biochemistry* **2003**, *42* (51), 15273–15283.
(22) Deniaud, A.; Rossi, C.; Berquand, A.; Homand, J.; Campagna, S.; Knoll, W.; Brenner, C.; Chopineau, J. Voltage-Dependent Anion Channel Transports Calcium Ions through Biomimetic Membranes. *Langmuir* **2007**, *23* (7), 3898–3905.
(23) Veneziano, R.; Rossi, C.; Chenal, A.; Devoisselle, J. M.; Ladant, D.; Chopineau, J. Bordetella Pertussis Adenylate Cyclase Toxin Translocation across a Tethered Lipid Bilayer. *PNAS* **2013**, *110* (51), 20473–20478.
(24) Koenig, J. V; Krueger, S.; Orts, W. J.; Majkrzak, C. F.; Berk, N. F.; Silverton, J. V; Gawrisch, K. Neutron Reflectivity and Atomic Force Microscopy Studies of a Lipid BIlayer in Water Adsorbed to the Surface of a Silicon Single Crystal. *Langmuir* **1996**, *12* (5), 1343–1350.
(25) Richter, R. P.; Bérat, R.; Brisson, A. R. Formation of Solid-Supported Lipid Bilayers: An Integrated View. *Langmuir* **2006**, *22* (8), 3497–3505. https://doi.org/10.1021/la052687c.
(26) Keller, C. A.; Glasmästar, K.; Zhdnov, V. P.; Kasemo, B. Formation of Supported Membranes from Veiscles. *Phys Rev Lett* **2000**, *84* (23), 5443–5446.
(27) Parkkila, P.; Viitala, T. Partitioning of Catechol Derivatives in Lipid Membranes: Implications for Substrate Specificity to Catechol-O-Methyltransferase. *ACS Chem Neurosci* **2020**, *11* (6), 969–978.
(28) Andersson, J.; Köper, I. Tethered and Polymer Supported Bilayer Lipid Membranes: Structure and Function. *Membr.* **2016**, *6* (2), 30.
(29) Sinner, E.; Ritz, S.; Naumann, R.; Schiller, S.; Knoll, W.; Gregory, S. M. Self-Assembled Tethered Bimolecular Lipid Membranes. *Adv Clin Chem* **2009**, *49*, 159–179.
(30) Tanaka, M.; Rosseti, F. F.; Kaufmann, S. Native Supported Membranes: Creation of Two-Dimensional Cell Membranes on Polymer Supports (Review). *Biointerphases* **2008**, *3* (2), FA12–FA16.
(31) Tanaka, M.; Sackmann, E. Polymer-Supported Membranes as Models of the Cell Surface. *Nature* **2005**, *437* (7059), 656–663.
(32) Köper, L.; Schiller, S. M.; Giess, F.; Naumann, R.; Knoll, W. *Advances in Planar Lipid Bilayers*

and Liposomes; Leitmannova Liu A, Ed.; Academic Press; Amsterdam, 2006; Vol. 3.
(33) Penkauskas, T.; Preta, G. Biological Applications of Tethered Bilayer Lipid Membranes. *Biochimie* **2019**, *157*, 131–141.
(34) Chadli, M.; Rebaud, S.; Maniti, O.; Tillier, B.; Cortès, S.; Girard-Egrot, A. New Tethered Phospholipid Bilayers Integrating Functional G-Protein-Coupled Receptor Membrane Proteins. *Langmuir* **2017**, *33* (39), 10385–10401. https://doi.org/10.1021/acs.langmuir.7b01636.
(35) Rossi, C.; Chopineau, J. Biomimetic Tethered Lipid Membranes Designed for Membrane-Protein Interaction Studies. *Eur Biophys J* **2007**, *36*, 955–965.
(36) Robelek, R.; Lemker, E. S.; Wiltschi, B.; Kirste, V.; Naumann, R.; Oesterhelt, D.; Sinner, E.-K. Incorporation of in Vitro Synthesized GPCR into a Tethered Artificial Lipid Membrane System. *Angew Chem Int Ed Engl* **2007**, *46* (4), 605–608.
(37) Rossi, C.; Doumiati, S.; Lazzarelli, C.; Davi, M.; Meddar, F.; Ladant, D.; Chopineau, J. A Tethered Bilayer Assembled on Top of Immobilized Calmodulin to Mimic Cellular Compartmentalization. *PLoS One* **2011**, *6* (4), e19101.
(38) Jackman, J. A.; Cho, N.-J. Model Membrane Platforms for Biomedicine: Case Study on Antiviral Drug Development. *Biointerphases* **2012**, *7* (1–4), 18.
(39) Coutable, A.; Thibault, C.; Chalmeau, J.; François, J. M.; Vieu, C.; Noireaux, V.; Trévisiol, E. Preparation of Tethered-Lipid Bilayers oń Gold Surfaces for the Incorporation of Integral Membrane Proteins Synthesized by Cell-Free Expression. *Langmuir* **2014**, *30* (11), 3132–3141.
(40) Maccarini, M.; Gayet, L.; Alcaraz, J.; Ligori, L.; Stidder, B.; Watkins, E. B.; Lenormand, J.; Martin, D. K. Functional Characterization of Cell-Free Expressed OprF Porin from Pseudomonas Aeruginosa Stably Incorporated in Tethered Lipid Bilayers. *Langmuir* **2017**, *33* (38), 9988–9996.
(41) S, W.; Kozuch, J.; Forbrig, E.; Tzschucke, C. C.; Jeuken, L. J. C.; Hildebrandt, P. Monitoring the Transmembrane Proton Gradient Generated by Cytochrome Bo3 in Tethered Bilayer Lipid Membranes Using SEIRA Spectroscopy. *J Phys Chem B* **2016**, *120* (9), 2249–2256.
(42) Rebaud, S.; Maniti, O.; Girard-Egrot, A. P. Tethered Bilayer Lipid Membranes (TBLMs): Interest and Applications for Biological Membrane Investigations. *Biochimie* **2014**, *107* (Part A), 135–142. https://doi.org/10.1016/j.biochi.2014.06.021.
(43) Alghalayini, A.; Garcia, A.; Berry, T.; Cranfield, C. G. The Use of Tethered Bilayer Lipid Membranes to Identify the Mechanisms of Antimicrobial Peptide Interactions with Lipid Bilayers. *Antibiot.* **2019**, *8* (1), 12.
(44) Yildiz, A. A.; Yildiz, U. H.; Liedberg, B.; Sinner, E. K. Biomimetic Membrane Platform: Fabrication, Characterization and Applications. *Colloids Surf, B* **2013**, *103*, 510–516.
(45) Zieleniecki, J. L.; Nagarajan, Y.; Waters, S.; Rongala, J.; Thompson, V.; Hrmova, M.; Köper, I. Cell-Free Synthesis of a Functional Membrane Transporter into a Tethered Bilayer Lipid Membrane. *Langmuir* **2016**, *32* (10), 2445–2449.
(46) Jackman, J. A.; Knoll, W.; Cho, N. J. Biotechnology Applications of Tethered Lipid Bilayer Membranes. *Materials (Basel).* **2012**, *5*, 2637–2657.
(47) Yildiz, A. A.; Kang, C. B.; Sinner, E. K. Biomimetic Membrane Platform Containing HERG Potassium Channel and Its Application to Drug Screening. *Analyst* **2013**, *138* (7), 2007–2012.
(48) Chadli, M.; Maniti, O.; Marquette, C.; Tillier, B.; Cortès, S.; Girard-Egrot, A.; Tilier, B.; Cortès, S.; Girard-Egrot, A. A New Functional Membrane Protein Microarray Based on Tethered Phospholipid Bilayers. *Analyst* **2018**, *143* (9), 2165–2173. https://doi.org/10.1039/c8an00260f.
(49) Reimhult, E.; Kumar, K. Membrane Biosensor Platforms Using Nano- and Microporous Supports. *Trends Biotchnol* **2008**, *26* (2), 82–89.
(50) Andersson, J.; Köper, I.; Knoll, W. Tethered Membrane Architectures—Design and Applications. *Front Mater* **2018**, *5* (55), 1–11.
(51) Munro, J. C.; Franck, C. W. In Situ Formation and Characterization of Poly(Ethylene Glycol)-Supported Lipid Bilayers on Gold Surfaces. *Langmuir* **2004**, *20* (24), 10567–10575.
(52) Andersson, J.; Knobloch, J. J.; Perkins, M. V; Holt, S. A.; Köper, I. Synthesis and

Characterization of Novel Anchorlipids for Tethered Bilayer Lipid Membranes. *Langmuir* **2017**, *33* (18), 4444–4451.

(53) Knoll, W.; Bender, K.; Förch, R.; Frank, C.; Götz, H.; Heibel, C.; Jenkins, T.; Jonas, U.; Kibrom, A.; Kügler, R.; Naumann, C.; Naumann, R.; Reisinger, A.; Rühe, J.; Schiller, S.; Sinner, E. K. Polymer-Tethered Bimolecular Lipid Membranes. In *Polymer Membranes/Biomembranes*; 2010; pp 87–111.

(54) Naumann, R.; Schmidt, E. K.; Joncyzk, A.; Fendler, K.; Kadenbach, B.; Liebermann, T.; Offenhäusser, A.; Knoll, W. The Peptide-Tethered Lipid Membranes as a Biomimetic System to Incoroporate Cytochrome c Oxidase in a Functionally Active Form. *Biosens Bioelectron* **1999**, *14* (7), 651–662.

(55) Naumann, R. L. C.; Knoll, W. Protein Tethered Lipid Bilayer: An Alternative Mimic of the Biological Membrane (Mini Review). *Biointerphases* **2008**, *3* (2), FA101–FA107.

(56) Giess, F.; Friedrich, M. G.; Heberle, J.; Naumann, R. L.; Knoll, W. The Protein-Tethered Lipid Bilayer: A Novel Mimic of the Biological Membrane. *Biophys J* **2004**, *87* (5), 3213–3220. https://doi.org/10.1529/biophysj.104.046169.

(57) Proux-Delrouye, V.; Elie, C.; Laval, J. M.; Loiroux, J.; Bourdillon, C. Formation of Tethered and Streptavidin-Supported Lipid Bilayers on a Microporous Electrode for the Reconstitution of Membranes of Large Surface Area. *Langmuir* **2002**, *18* (8), 3263–3272.

(58) Berquand, A.; Mazeran, P. E.; Pantigny, J.; Proux-Delrouye, V.; Laval, J. M.; Bourdillon, C. Two-Step Formation of Streptavidin-Supported Lipid Bilayers by PEG-Triggered Vesicle Fusion. Fluorescence and Atomic Force Microscopy Characterization. *Langmuir* **2003**, *19* (5), 1700–1707.

(59) Taylor, J. D.; Linman, M. J.; Wilkop, T.; Cheng, Q. Regenerable Tethered Bilayer Lipid Membrane Arrays for Multiplexed Label-Free Analysis of Lipid-Protein Interactions on Poly(Dimethylsiloxane) Microchips Using SPR Imaging. *Anal Chem* **2009**, *81* (3), 1146–1153.

(60) Elie-Caille, C.; Fliniaux, O.; Pantigny, J.; Mazière, J. C.; Bourdillon, C. Self-Assembly of Solid-Supported Membranes Using a Triggered Fusion of Phospholipid-Enriched Proteoliposomes Prepared from the Inner Mitochondrial Membrane. *Langmuir* **2005**, *21* (10), 4661–4668.

(61) Sumino, A.; Dewa, T.; Takeuchi, T.; Sugiura, R.; Sasaki, N.; Misawa, N.; Tero, R.; Urisu, T.; Gardiner, A. T.; Cogdell, R. J.; Hashimoto, H.; Nango, M. Construction and Structural Analysis of Tethered Lipid Bilayer Containing Photosynthetic Antenna Proteins for Functionnal Analysis. *Biomacromolecules* **2011**, *12* (7), 2850–2858.

(62) Junghans, A.; Köper, I. Structural Analysis of Tethered Bilayer Lipid Membranes. *Langmuir* **2010**, *26* (13), 11035–11040.

(63) Leitch, J.; Kunze, J.; Goddard, J. D.; Schwan, A. L.; Faragher, R. J.; Naumann, R.; Knoll, W.; Dutcher, J. R.; Lipkowski, J. In Situ PM-IRRAS Studies of an Archaea Analogue Thiolipid Assembled on a Au(111) Electrode Surface. *Langmuir* **2009**, *25* (17), 10354–10363. https://doi.org/10.1021/la900907d.

(64) Naumann, R.; Baumgart, T.; Gräber, P.; Jonczyk, A.; Offenhäusser, A.; Knoll, W. Proton Transport through a Peptide- Tethered Bilayer Lipid Membrane by the H+-ATP Synthase from Chloroplasts Measured by Impedance Spectroscopy. *Biosens Bioelectron* **2002**, *17* (1–2), 25–34.

(65) Bunjes, N.; Schmidt, E. K.; Joncyzk, A.; Rippmann, F.; Beyer, D.; Ringsdorf, H.; Gräber, P.; Knoll, W.; Naumann, R. Thiopeptide-Supported Lipid Layers on Solid Substrates. *Langmuir* **1997**, *13* (23), 6188–6194.

(66) Schmidt, E. K.; Liebermann, T.; Kreiter, M.; Joncyzk, A.; Naumann, R.; Offenhäusser, A.; Neumann, E.; Kukol, A.; Maelicke, A.; Knoll, W. Incorporation of the Acetylcholine Receptor Dimer from Torpedo Californica in a Peptide Supported Lipid Membrane Investigated by Surface Plasmon and Fluorescence Spectroscopy. *Biosens Bioelectron* **1998**, *13* (6), 585–591.

(67) Girard-Egrot, A. P.; Maniti, O. Why Do Tethered-Bilayer Lipid Membranes Suit for Functional Membrane Protein Reincorporation? *Appl. Sci.* **2021**, *11* (11), 4876. https://doi.org/10.3390/app11114876.

(68) Yildiz, A. A.; Knoll, W.; Gennis, R. B.; Sinner, E. K. Cell-Free Synthesis of Cytochrome Bo(3) Ubiquinol Oxidase in Artificial Membranes. *Anal Biochem* **2012**, *423* (1), 39–45.
(69) Naumann, R.; Jonczyk, A.; Kopp, R.; van Esch, J.; Ringsdorf, H.; Knoll, W.; Gräber, P. Incorporation of Membrane Proteins in Solid-Supported Lipid Layers. *Angew Chem Int Ed Engl* **1995**, *34* (18), 2056–2058.
(70) Sinner, E. K.; Reuning, U.; Kök, F. N.; Sacca, B.; Moroder, L.; Knoll, W.; Oesterhelt, D. Incorporation of Integrins into Artificial Planar Lipid Membranes: Characterization by Plasmon-Enhanced Fluorescence Spectroscopy. *Anal Biochem* **2004**, *333* (2), 216–224.
(71) Girard-Egrot, A.; Maniti, O.; Rebaud, S. Substrate/Peptide/Lipid Bilayer Assembly, Preparation Methods and Associated Detection Methods. International Patent WO/2016/066947, 2016.
(72) Elazar, M.; Cheong, K. H.; Liu, P.; Greenberg, H. B.; Rice, C. M.; Glenn, J. S. Amphipathic Helix-Dependent Localization of NS5A Mediates Hepatitis C Virus RNA Replication. *J. Virol.* **2003**, *77* (10), 6055–6061. https://doi.org/10.1128/jvi.77.10.6055-6061.2003.
(73) Cho, N. J.; Frank, C. W.; Kasemo, B.; Höök, F. Quartz Crystal Microbalance with Dissipation Monitoring of Supported Lipid Bilayers on Various Substrates. *Nac Protoc* **2010**, *5* (6), 1096–1106.
(74) Cho, N. J.; Cho, S. J.; Kwang, H. C.; Glenn, J. S.; Frank, C. W. Employing an Amphipathic Viral Peptide to Create a Lipid Bilayer on Au and TiO2. *J. Am. Chem. Soc.* **2007**, *129* (33), 10050–10051. https://doi.org/10.1021/ja0701412.
(75) Cho, N. J.; Cho, S. J.; Hardesty, J. O.; Glenn, J. S.; Frank, C. W. Creation of Lipid Partitions by Deposition of Amphipathic Viral Peptides. *Langmuir* **2007**, *23* (21), 10855–10863. https://doi.org/10.1021/la700640h.
(76) Cho, N.-J. J.; Wang, G.; Edvardsson, M.; Glenn, J. S.; Hook, F.; Frank, C. W.; S. Glenn, J.; Hook, F.; W. Frank, C.; Glenn, J. S.; Hook, F.; Frank, C. W.; S. Glenn, J.; Hook, F.; W. Frank, C. Alpha-Helical Peptide-Induced Vesicle Rupture Revealing New Insight into the Vesicle Fusion Process As Monitored in Situ by Quartz Crystal Microbalance-Dissipation and Reflectometry. *Anal. Chem.* **2009**, *81* (12), 4752–4761. https://doi.org/10.1021/ac900242s.
(77) Wallin, M.; Choi, J.-H.; Kim, S. O.; Cho, N.-J.; Andersson, M. Peptide-Induced Formation of a Tethered Lipid Bilayer Membrane on Mesoporous Silica. *Eur. Biophys. J.* **2015**, *44* (1), 27–36. https://doi.org/10.1007/s00249-014-0998-1.
(78) Zan, G. H.; Jackman, J. A.; Cho, N.-J. AH Peptide-Mediated Formation of Charged Planar Lipid Bilayers. *J. Phys. Chem. B* **2014**, *118* (13), 3616–3621. https://doi.org/10.1021/jp411648s.
(79) Hardy, G. H.; Nayak, R.; Alam, S. M.; Shapter, J. G.; Heinrich, F.; Zauscher, S. Biomimetic Supported Lipid Bilayers with High Cholesterol Content Formed by α-Helical Peptide-Induced Vesicle Fusion. *J Mater Chem* **2012**, *22* (37), 1956–19513.
(80) Cho, N.-J.; Dvory-Sobol, H.; Xiong, A.; Cho, S.-J.; Frank, C. W.; Glenn, J. S. Mechanism of an Amphipathic α-Helical Peptide's Antiviral Activity Involves Size-Dependent Virus Particle Lysis. *ACS Chem. Biol.* **2009**, *4* (12), 1061–1067. https://doi.org/10.1021/cb900149b.
(81) Koldso, H.; Shorthouse, D.; Hélie, J.; Sansom, M. S. P. Lipid Clustering Correlates with Membrane Curvature as Revealed by Molecular Simulations of Complex Lipid Bilayers. *PLoS Comput Biol* **2014**, *10* (10), e1003911.
(82) Wiltschi, B.; Knoll, W.; Sinner, E. K. Binding Assays with Artificial Tethered Membranes Using Surface Plasmon Resonance. *Methods* **2006**, *39* (2), 134–146.
(83) Munguira, I.; Casuso, I.; Takahashi, H.; Rico, F.; Miyagi, A.; Chami, M.; Scheuring, S. Glasslike Membrane Protein Diffusion in a Crowded Membrane. *ACS Nano* **2016**, *10* (2), 2584–2590.
(84) Ausserré, D.; Valignat, M. P. Wide-Field Optical Imaging of Surface Nanostructures. *Nano Lett* **2006**, *6* (7), 1384–1388.
(85) Campidelli, S.; Aboukhachfe, R.; Jaouen, K.; Monteiller, J.; Amra, C.; Zerrad, M.; Cornut, R.; Derycke, V.; Ausserré, D. Backside Absorbing Layer Microscopy: Watching Graphene Chemistry. *Sci Adv* **2017**, *3* (5), e1601724.
(86) Ausserre, D.; Abou Khachfe, R.; Roussille, L.; Brotons, G.; Vonna, L.; Lemarchand, F.; Zerrad, M.; Amra, C. Anti-Reflecting Absorbing Layers for Electrochemical and Biophotonic

Applications. *J Nanomed Nanotechnol* **2014**, *5* (4), 2–6.
(87) Theodody, O.; Garcia-Seyda, N.; Bedu, F.; Luo, X.; Gabriele, S.; Mignot, T.; Giermanska, J.; Chapel, J. P.; Metivier, M.; Valignat, M. P. Live Nanoscopic to Mesoscopic Topography Reconstruction with an Optical Microscope for Chemical and Biological Samples. *PLoS One* **2018**, *13* (12), e0207881.
(88) Gunnarsson, A.; Bally, M.; Jönson, P.; Médard, N.; Höök, F. Time-Resolved Surface-Enhanced Ellipsometric Contrast Imaging for Label-Free Analysis of Biomolecular Recognition Reactions on Glycolipid Domains. *Anal Chem* **2012**, *84* (15), 6538–6545.
(89) Ducret, A.; Valignat, M. P.; Mouhamar, F.; Mignot, T.; Theodody, O. Wet-Surface-Enhanced Ellipsometric Contrast Microscopy Identifies Slime as a Major Adhesion Factor during Bacterial Surface Motility. *Proc Natl Acad Sci USA* **2012**, *109* (25), 10036–10041.
(90) Lemineur, J. F.; Noëm, J. M.; Ausserré, D.; Combellas, C.; Kanoufi, F. Combining Electrodeposition and Optical Microscopy for Probing Size-Dependent Single Nanoparticle Electrochemistry. *Angew Chem int Ed* **2018**, *57* (37), 11998–12002.
(91) Abou Khachfe, R.; Ausserré, D. Backside Absorbing Layer Microscopy: A Universal Relationship between Physical Thickness and Reflectivity. *Opt Express* **2020**, *28* (4), 4836–4844.
(92) Bompard, J.; Rosso, A.; Brizuela, L.; Mebarek, S.; Blum, L. J.; Trunfio-Sfarghiu, A. M.; Lollo, G.; Granjon, T.; Girard-Egrot, A.; Maniti, O. Membrane Fluidity as a New Means to Selectively Target Cancer Cells with Fusogenic Lipid Carriers. *Langmuir* **2020**, *36* (19), 5134–5144. https://doi.org/10.1021/acs.langmuir.0c00262.
(93) Cho, N. J.; Cho, S. J.; Kwang, H. C.; Glenn, J. S.; Frank, C. W. Employing an Amphipatic Viral Peptide to Create a Lipid Bilayer on Au and TiO2. *J Am Chem Soc* **2007**, *129* (33), 10050–10051.
(94) Gray, G. M.; Yardley, H. J. Lipid Compositions of Cells Isolated from Pig, Human, and Rat Epidermis. *J Lipid Res* **1975**, *16* (6), 434–440.
(95) Spector, A. A.; Yorek, M. A. Membrane Lipid Composition and Cellular Function. *J Lipid Res* **1985**, *26* (9), 1015–1035.
(96) Pankov, R.; Markovska, T.; Antonov, P.; Ivanova, L.; Momchilova, A. The Plasma Membrane Lipid Composition Affects Fusion between Cells and Model Membranes. *Chem Biol Interact* **2006**, *164* (3), 167–173.
(97) Virtanen, J. A.; Cheng, K. H.; Somerharju, P. Phospholipid Composition of the Mammalian Red Cell Membrane Can Be Rationalized by a Superlattice Model. *Proc Natl Acad Sci USA* **1998**, *95* (9), 4964–4969.
(98) S, J. L.; Campbell, C. T.; Chinowsky, T. M.; Mar, M. N.; Yee, S. S. Quantitative Interpretation of the Response of Surface Plasmon Resonance Sensors to Adsorbed Films. *Langmuir* **1998**, *14* (19), 5636–5648.
(99) Parkkila, P.; Elderfi, M.; Bunker, A.; Viitala, T. Biophysical Characterization of Supported Lipid Bilayers Using Parallel Dual-Wavelength Surface Plasmon Resonance and Quartz Crystal Microbalance Measurements. *Langmuir* **2018**, *34* (27), 8081–8091.
(100) Winsel, K.; Hönig, D.; Lunkenheimer, K.; Geggel, K.; Witt, C. Quantitative Brewster Angle Microscopy of the Surface Film of Human Broncho-Alveolar Lavage Fluid. *Eur Biophys J* **2003**, *32* (6), 544–552.
(101) Jackman, J. A.; Zan, G. H.; Zhdanov, V. P.; Cho, N. J. Rupture of Lipid Vesicles by a Broad-Spectrum Antiviral Peptide: Influence of Vesicle Size. *J Phys Chem B* **2013**, *117*, 16117–16128.
(102) Inkpen, M. S.; Liu, Z. F.; Li, H.; Campos, L. M.; Neaton, J. B.; Venkataraman, L. Non-Chemisorbed Gold-Sulfur Binding Prevails in Self-Assembled Monolayers. *Nat Chem* **2019**, *11* (4), 351–358.

TOC figure

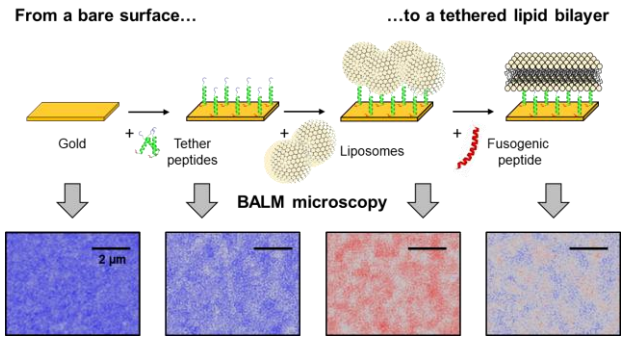
From a bare surface...
...to a tethered lipid bilayer
Gold
Tether peptides
Liposomes
Fusogenic peptide
BALM microscopy
2 µm